

Copyright © 1992, by the author(s).  
All rights reserved.

Permission to make digital or hard copies of all or part of this work for personal or classroom use is granted without fee provided that copies are not made or distributed for profit or commercial advantage and that copies bear this notice and the full citation on the first page. To copy otherwise, to republish, to post on servers or to redistribute to lists, requires prior specific permission.

**RF DISCHARGE IMPEDANCE MEASUREMENTS  
AND COMPARISON TO A DISCHARGE MODEL**

by

A. H. Sato and M. A. Lieberman

Memorandum No. UCB/ERL M92/34

7 April 1992

**RF DISCHARGE IMPEDANCE MEASUREMENTS  
AND COMPARISON TO A DISCHARGE MODEL**

by

A. H. Sato and M. A. Lieberman

Memorandum No. UCB/ERL M92/34

7 April 1992

**ELECTRONICS RESEARCH LABORATORY**

College of Engineering  
University of California, Berkeley  
94720

# **RF Discharge Impedance Measurements and Comparison to a Discharge Model**

**A.H. Sato**

Department of Physics, University of California, Berkeley, CA 94720

**M.A. Lieberman**

Department of Electrical Engineering and Computer Sciences  
University of California, Berkeley, CA 94720

## **ABSTRACT**

RF current measurements have been conducted on an asymmetric capacitive discharge in argon at pressures of 3.7 to 70 mtorr, at 10 MHz, over a voltage amplitude range of -100 V to -700 V. Confinement of the glow between the powered electrode and a well-defined grounded electrode was found to be essential for measurements of the rf current flowing to the grounded electrode. With our previous axial electric field measurements in the glow [A.H. Sato and M.A. Lieberman, J. Appl. Phys. **68**, 6117 (1990)], the current measurements provide further evidence indicating that the glow impedance has a negative real part for argon discharges up to pressures of at least 20 mtorr.

The current and voltage waveforms were Fourier transformed to study the discharge impedance. The first harmonic current amplitude  $I$  was found to vary nearly linearly with the first harmonic voltage amplitude  $V_{rf}$ , and the discharge power was found to vary nearly quadratically with  $V_{rf}$ . The data also showed that a small amount of power is emitted from the discharge at the second harmonic.

A simple discharge model was developed to study the effect of secondary electrons on the

discharge behavior, and also to study recent ideas on the dc bias that appears in asymmetric discharges. The model describes the discharge in terms of an equivalent circuit, using self-consistent sheath model results for the sheath impedance, and the cold plasma description for the glow impedance. Particle balance and electron power balance are combined to determine values for the electron temperature and plasma density, and values for the sheath and glow impedances can be obtained with these. Two versions of the discharge model are developed for the cases of collisionless and collision-dominated ion transport through the sheaths. The discharge model includes stochastic sheath heating, glow ohmic heating and secondary electron power to provide energy to the electrons. Using stochastic and ohmic heating alone in the model gives a sublinear  $I - V_{rf}$  relation. Adding secondary electron power improves the linearity of  $I$  vs.  $V_{rf}$ . Good agreement with experimental  $I - V_{rf}$  data is obtained with effective secondary electron emission coefficients  $\gamma_{eff}$  of 0.03, 0.08, and 0.16 at 3.7, 20, and 70 mtorr, respectively. The total discharge power obtained using these values for  $\gamma_{eff}$  agrees well with experimental data, even though a fit of the rf current data does not automatically imply agreement in the power data. The dc bias results from the collisional sheath version of the model are close to the 20 and 70 mtorr experimental data. Differences of -16% are observed in the slopes of the model and experimental  $V_{dc}$  vs.  $V_{rf}$  lines. The slope of  $V_{dc}$  vs.  $V_{rf}$  for the 3.7 mtorr experimental data is ~34% lower than results from the collisionless version of the model. The larger discrepancy in this case may indicate the influence of the glow shape on the electrical asymmetry of the discharge.

## I. Introduction

In capacitive rf discharges, at pressures below a few hundred millitorr, the interaction of electrons with the time-varying fields in the sheath regions are an important mechanism for creating energetic electrons. This heating mechanism depends not only on the sheath electric fields, but also on the glow electric field, as the latter determines the flux of slow electrons incident upon the sheath. Sommerer et al.<sup>1</sup> studied the effect of temporarily inverting or zeroing the glow electric field for a few rf cycles in a self-consistent kinetic model of helium rf discharges. The self-consistent glow electric field normally decelerates fast (~15 eV) electrons as they approach an expanding sheath. Inverting the sign of the glow electric field, or setting it to zero, allows the fast electrons to impinge upon the expanding sheath, and the simulations showed that the electron heating was enhanced and that the total ionization increased by 20% over one rf period.

Our interest in rf sheaths led us to perform electric field measurements in the sheath and glow region in capacitive rf argon discharges.<sup>2</sup> One effect we observed was an anomalous phase shift of the glow electric field with respect to the voltage across the two electrodes. This suggested that electrons could be cooled in the glow region; that is, the time-averaged product of the current and glow electric field --  $\langle I(t)E_{\text{glow}}(t) \rangle$  -- was negative. This particular observation led to our efforts to measure the discharge current. These experiments are presented in this paper.

The rf current measurements had an additional benefit: They allow one to study the discharge impedance and experimentally test this aspect of rf discharge models. The models, in turn, serve to clarify the processes occurring in the discharge, as well as the electrostatic behavior of the discharge. Previous impedance studies tried to indirectly measure the plasma parameters such as the plasma density,<sup>3</sup> elastic scattering frequency,<sup>4</sup> or the sheath voltage and glow electric field.<sup>5</sup> Also, under certain conditions it is possible to experimentally isolate a single energy deposition process. For example, at pressures higher than ~100mt, one can distinguish the ohmic heating from the ion power if a wide current range is available.<sup>6</sup> At lower pressures this separation is more difficult because electron energy conservation balance involves the additional mechanism of stochastic heating. However, the sum of the ohmic and stochastic heating powers can be determined.<sup>7</sup> Or, at lower voltages the stochastic heating term can be experimentally distinguished from the

ohmic heating term,<sup>8,9</sup> but above  $\sim 100$  V the ion power contribution to the total discharge power is significant and this makes separating the stochastic heating term difficult. In general, such convenient situations may not exist for the pressure and voltage range of a particular application. Under these circumstances a global discharge model is especially helpful in understanding discharge behavior.

In recent years it has been recognized that measuring the impedance of capacitive rf discharges can be difficult. In electropositive gas discharges, the phase shift  $\theta$  between the current and voltage is nearly  $90^\circ$ , and at 10 MHz  $90^\circ - \theta$  can amount to only 1 ns of shift in time. This can be difficult to measure accurately. Additionally, it has been recognized that most of the power from the rf generator can be dissipated in matching networks employed in the external circuit,<sup>10,11</sup> and hence nominal power measurements provided by directional wattmeters can be misleading, and hence not an easily interpretable variable against which to correlate plasma parameters. Thus, accurate measurements of external variables -- current, voltage, or power -- are difficult to realize, but are important for careful experimental work on rf discharges. This has motivated extensive efforts to establish reliable practices for measuring discharge impedance. Such is typified by the recent work on the GEC Reference Cell,<sup>12</sup> and also by the many papers devoted to increasing the accuracy of power measurements by calibration with dummy loads,<sup>13</sup> or by the use of methods which attempt to subtract power losses in cabling and the matching network from the total power delivered by the rf generator.<sup>11,14</sup> These methods are difficult to employ reliably, and debate has centered on whether all stray power losses have been fully accounted for in the matching network and cabling.<sup>15</sup> Consequently, many workers now prefer to compute the power from the time-averaged product of the measured current and voltage waveforms.<sup>12,16</sup> Much of this work has been done on fairly symmetric systems in glass vessels. We have tried to employ this technique on our asymmetric discharge in a metal chamber and found that our current waveforms exhibit a skewness not present in symmetric discharge results.

In our asymmetric system we encountered difficulties in measuring the discharge current. Harmonic content is enhanced for asymmetric systems, and this worsens the ever-present problem of resonances and parasitic oscillations in the apparatus. It is important to design the electrode configuration properly to facilitate the current measurement. The final electrode design is discussed in this paper. We also found it

was important to perform the current measurement in a way that was insensitive to parasitic current oscillations, and in a way that ensured discharge confinement. These two features of the experiment were crucial, and are discussed in this paper. These problems are less severe in much of the work in symmetric systems. First, the symmetry implies smaller harmonic content in the current, and hence, less concern for the frequency response of the external circuit at higher harmonics. Second, much of this work was done in glass vessels. This makes parasitic oscillations -- currents circulating in the ground plane -- less likely, and hence, these stray current oscillations are less of a problem. We note however, even in such systems, if the discharge symmetry is destroyed by the escape of the glow from confinement (it may spread into the gas feed lines or pumping ports) the discharge current will again exhibit large harmonic content.<sup>17,18</sup> An escape of the glow can be initiated by arc formation occurring at large rf voltages. Hence, these symmetric, glass systems are not immune to the problems we also encountered, but rather avoid these problems by considering them outside the voltage range of interest.

This paper is organized as follows: Section II describes the apparatus and experimental procedure for the rf current measurements in our asymmetric system. In Section III the experimental results are presented and discussed in relation to experimental results obtained by other workers. Section IV presents a simple model of an asymmetric capacitive rf discharge. This model is an adaptation of the work of Misium et al.<sup>19</sup> augmented by electrode asymmetry and a radially nonuniform plasma. In Section V the model results are presented and discussed with respect to the experimental results and also other modeling works. Section VI gives some general comments about the model validity and remaining issues. Section VII closes with a summary of this paper.

## II. Experimental Method

### A. Electrode Configuration

Figure 1 shows a schematic of the vacuum chamber, the electrode configuration, and the current and voltage probes. In the original configuration, the grounded electrode GE2 and its supports are not present. The vacuum chamber is a 12 inch inner diameter aluminum cylindrical vessel that is closed off at both ends

by movable aluminum pistons. The chamber wall and pistons are nominally at ground potential. 9 inch diameter electrodes seal off each piston, and consist of 3/4 inch thick aluminum disks covered by 1/8 inch thick copper disks that act as the exposed surfaces. Both electrodes are set off from the pistons by teflon spacers. During operation one electrode (GE1) is grounded to its supporting piston, and the other electrode (the powered electrode) is driven by the rf power supply through an L type matching network. A grounded guard electrode is placed around the circumference of the powered electrode to prevent the formation of a glow along the radial surface of the electrode. The guard electrode is a band of 1/16 inch thick copper formed in a ring of -9.3 inch inner diameter.

Preliminary current measurements for argon discharges at 3 and 20 mtorr, with an electrode spacing of 3 inches, were made using the basic configuration described above. The current at the grounded electrode was measured with a Pearson 2877 current monitor placed on a short 1/4 inch diameter rod mounted at the center of the atmospheric side of the grounded electrode. The connection to ground was completed through three 2.5 inch wide copper bands, in order to minimize ground loop inductance. In this configuration the measured current exhibited harmonic distortions which occasionally caused the time-averaged product of this current with the voltage at the powered electrode to be negative. At the low pressures used, the glow spreads beyond the region between the electrodes. Tochikubo et al.<sup>20</sup> reported that an unconfined glow can lead to large harmonic content in the current measured at the grounded electrode. This effect may be due to oscillations excited by nonlinearities in the sheath which circulate rf current from the glow into the grounded electrode, through a small (but nonzero) ground loop inductance to the chamber side wall, and finally back through the side wall sheath into the glow. Near resonant behavior between the sheath capacitances and the ground loop inductance has been used deliberately in substrate rf biasing<sup>21,22</sup> and it is possible for the small ground loop inductance to contribute to similar parasitic oscillations at harmonics of the driving voltage. The problem with this parasitic current is that it does not flow from the powered to grounded electrode, and therefore confuses the time-averaged current and voltage product.

A more desirable electrode configuration is one which further reduces the inductance between two points on the grounded electrode, and permits a measurement which reflects only the current that actually

flows from the powered to grounded electrode. A new ground electrode, formed from the side and bottom of a cylindrical cavity, was installed for this purpose (see GE2 in Fig. 1). The inner diameter was 9.3 inches and its axial length was 2.5 inches. The purely geometric area ratio of the grounded and powered electrodes was therefore 2.1. The new grounded electrode was fabricated out of 0.025 inch thick copper sheet, and was isolated from -- and supported by -- the original grounded electrode by four 0.75 inch high teflon spacers. The current return path was a single 2 inch wide ground strap that was connected to a vacuum feedthrough constructed of a 0.25 inch diameter rod passing through a plexiglass flange. The clearance from the rod to the chamber wall was 0.75 inch. The current monitor was mounted on the rod on the atmospheric side of the feedthrough, and the end of the rod was connected by a 2 inch wide strap to the vacuum chamber wall at the base of the plexiglass flange.

The powered and grounded electrodes were positioned to form a cylindrical cavity, with a 0.1 inch gap between the grounded and powered electrode to accommodate misalignments. In this arrangement, the glow could be confined for argon pressures up to 70 mtorr and rf voltage amplitudes of 700 V. At much higher pressures or voltages the glow would spread out from the gap separating the two electrodes. When this happened, the dc bias on the powered electrode increased from 1/2 of the rf amplitude to 4/5 of the rf amplitude, implying significant current was flowing to other parts of the vacuum vessel and that the discharge had become more asymmetric. The data to be presented was obtained when the glow remained confined to the cylindrical cavity.

## B. Current and Voltage Measurements

The rf voltage is measured with a capacitive divider positioned at the N type rf connector that connects directly to the powered electrode. This yields the voltage of the powered electrode with respect to the chamber wall ground; this is the sum of the voltage between the powered and grounded electrodes, as well as the voltage drop across the high frequency impedance of the ground strap connecting the ground electrode to the chamber wall. The inductance from the ground electrode to the chamber wall was measured as 90 nH at 10 MHz, and this give a reactance of 6 ohm at 10 MHz. Since the discharge reactance is greater than 300

ohms in magnitude, the rf voltage will be in error by only a few percent in magnitude.

The current and voltage waveforms were measured simultaneously with two gated integrator and boxcar averager modules, as shown in Fig. 2. Waveform samples were taken at 1 ns intervals, nominally, and exponential averaging was used for each sample to reduce jitter in the data sets. In this arrangement, the first boxcar triggers the second boxcar. The two modules do not use exactly the same increment in time between samplings, so that the time axis of the data set from one boxcar module is rescaled by an appropriate factor. This factor was found by feeding a common sinusoidal wave train to both boxcar modules from a signal generator, and noting the ratio of the number of samples between zero crossings for the two data sets. This calibration also provides the time delay between data sets taken by the two boxcar modules that results from the triggering scheme used. The signal generator must be well warmed-up and stable to avoid drifts in the period of the calibration signal.

The current signal is sent from the current monitor through a 50 ohm terminated coaxial cable to the boxcar module input. The output of the capacitive divider is monitored with a 10X probe which is connected to the second boxcar module. The difference in propagation time for the signals on these two cabling paths was found by using a sinusoidal test signal imposed across a teflon dielectric capacitor. The tangent of the loss angle for teflon<sup>23</sup> at 10 MHz is equivalent to only a few picoseconds of time shift between the current and voltage waveforms. This is below the phase error introduced by sampling jitter of ~0.1 ns. Therefore, in this calibration we determine the difference in cable propagation time by requiring the current to lead the voltage by 90°. This calibration was done for the 10 MHz (first harmonic component) results reported in Section III.

### III. Experimental Results and Discussion

#### A. The Discharge Current

Figure 3 shows sample current waveforms. Fig. 3a shows an early attempt to measure the discharge current  $I(t)$  for a 30 mtorr, 600 V argon discharge in the original electrode configuration. The electrode spacing was 3 inches and the cylindrical grounded electrode was absent, thus allowing the glow to spread

throughout the vacuum chamber. The rf frequency was 13.6 MHz. The discharge current  $I(t)$  was calculated. In this method, the total current  $I_{\text{tot}}(t)$  entering the powered electrode was measured with a current transformer mounted near the capacitive divider (see Fig. 1). The stray capacitance from the powered electrode to the guard electrode was measured as  $C_s \approx 138$  pf, and the current drawn by this capacitance was calculated as  $C_s dV/dt$  using the measured voltage waveform. The discharge current was then calculated with  $I = I_{\text{tot}} - C_s dV/dt$ .

This method generally gave skewed waveforms for  $I(t)$ , as shown in Fig. 3a, for other pressures down to -3 mtorr. Since the glow was unconfined, the discharge was highly asymmetric. The dc bias for the case of Fig. 3a was -600V. The skewed nature of  $I(t)$  is due to the discharge asymmetry.

Figure 3a illustrates a difficulty with the original method of measuring  $I(t)$ : The desired waveform is the difference of two large waveforms of nearly the same size. Thus, extracting  $I(t)$  is sensitive to errors in time shifts between  $I_{\text{tot}}$  and  $C_s V/dt$  (or  $V(t)$ ). At 3 mtorr the discharge current was even a smaller fraction of the stray current, and this method was even more difficult to use than at 30 mtorr.

This method was suitable for observing qualitative features of  $I(t)$  such as amplitude and skewness. But it was not accurate enough to compute the discharge power. Data obtained with the confined glow scheme (described in Section II) showed that the phase shift  $\theta$  of the  $I(t)$  with respect to the  $V(t)$  was  $-87^\circ$  at the first harmonic. Adding a stray capacitance that draws -5 times as much current as the discharge decreases the difference  $90^\circ - \theta$  to a level comparable to timing errors introduced by the instrumentation ( $-0.1\text{ns} - 0.5^\circ$  at 13.6 MHz). The discharge power is proportional to  $\cos \theta = \sin(90^\circ - \theta)$ , thus errors introduced in measuring the phase of the impedance at the powered electrode were comparable to the power factor  $\cos \theta$  itself.

The confined glow scheme was developed to remedy this problem. By measuring the rf current at the grounded electrode, the effect of the large stray current (in parallel with the powered electrode) on the phase shift between the discharge current and voltage is minimized.<sup>6</sup> Figure 3b shows a current waveform for the 20 mtorr, 600V discharge when the glow is confined inside the cylindrical ground electrode. The rf frequency was lowered to 10 MHz to provide a larger rf period and greater tolerance of timing errors. Once again  $I(t)$

is skewed. The phase shift between the measure current and voltage waveforms is larger, however, and this aids the computation of the discharge power.

In both Fig. 3a and 3b, a high frequency oscillation is visible. We believe this oscillation is due to a resonance in the external circuit since the prominent frequency did not seem to change with plasma conditions. (Note that in both examples the period is roughly 20 ns, despite the change in rf frequency and plasma parameters.)

These measurements show that the current waveforms in the original chamber configuration are skewed sine waves having a capacitive relation to the voltage waveform. The original method of computing  $I(t)$  is capable of demonstrating this, although precise determination of the phase relation between  $I(t)$  and  $V(t)$  is not possible. However, even with this small uncertainty in phase shift, these current measurements and our previous electric field measurements<sup>2</sup> show that the glow impedance has a negative real part; that is,  $\langle I(t)E_{\text{glow}}(t) \rangle - R_{\text{glow}} I_{\text{rms}}^2 < 0$ . This is shown in Fig. 4 for the 2.3 mtorr. Current waveforms obtained from the original method of computing  $I(t)$  are shown with measurements of the axial electric field in the glow. A visual estimate of the product of these two show that the product will be negative. In this argument the measured external current is assumed to be equal to the glow conduction current. Initially we sought to check current continuity by measuring the current waveform at both the powered and grounded electrode (see Section IIA above) but encountered the problem of parasitic current oscillations. The confined glow experiments indicate that the skewed, sinusoidal nature of the current waveform is preserved across the discharge. Our recently developed two-coupled-sheath model<sup>24</sup> for current conduction through a capacitive discharge also supports the essential features of our current measurements. We also note that recent theory and simulation work by Surendra et al.<sup>25</sup> supports the possibility of a negative glow resistance.

## B. The Discharge Impedance

Figures 5 to 7 show experimental data points for argon discharges driven by a 10 MHz external voltage obtained in the confined glow scheme. The pressures used were 3.7, 20 and 70 mtorr. The dc bias, the first harmonic current amplitude (now denoted by  $I$ ), and the discharge power are plotted as functions of the first

harmonic voltage amplitude  $V_{rf}$ . Also shown are curves obtained from the discharge model to be described in Section IV.

Figure 5a shows the dc bias for the 3.7 mtorr discharge. In this graph and in the dc bias plots for the 20 mtorr (Fig. 6a) and 70 mtorr (Fig. 7a) cases, the experimental dc bias is fairly linear with the rf voltage, and a line through the data passes below the origin at  $V_{rf} = 0$ . In Ref. 24 we showed that the dc bias varies quadratically with  $V_{rf}$  at small  $V_{rf}$ . Also,  $V_{dc}$  should be bounded from above by the curve for infinite area ratio,  $V_{dc} = (kT_e/e) \ln( I_0(eV/kT_e) )$ , where  $I_0$  is the modified Bessel function.<sup>26</sup> Thus, for small  $V_{rf}$  the dc bias should vanish more quickly than linearly. This is consistent with the experimental dc bias data shown here.

The first harmonic amplitude data was obtained by Fourier transforming the waveforms after correcting the two data sets for sampling time interval differences and cable propagation time differences. The power reported is actually the sum of products of the Fourier coefficients for the first 10 harmonics. For this quantity, the higher harmonics are much smaller than the power at the first harmonic, since each higher harmonic amplitude is roughly a factor of 10 or more smaller than the fundamental. Sample current and voltage spectra are shown in Fig. 8 for a 70 mtorr, 700 V discharge. This was typical of all the discharge cases. The current spectrum extends to the fifth to eighth harmonic. The amplitudes of the second harmonic and above are a factor of 10 or more smaller than the fundamental, except for a resonance that may be excited at the fifth or sixth harmonic. The voltage spectrum drops off quickly, with only a significant second harmonic that is still at least a factor of 10 smaller than the fundamental. Other workers have corrected their measurements for the frequency response of the electronics at higher harmonics,<sup>12</sup> however this would not be a large correction here, and was therefore not performed.

Two data sets taken several weeks apart are shown for the 20 and 70 mtorr cases, and demonstrate the reproducibility of the data. The scatter in the discharge power is due to jitter in measurements of the phase shift between the voltage and current waveforms. The spread in the phase shift was as large as  $-0.6^\circ$  for the 70 mtorr data, and this was consistent with the gate jitter of the gated integrator modules.

The  $I - V_{rf}$  relations were all closely linear for each of the three pressures. A logarithmic fit gave  $I - V^n$

where  $n \approx 0.98, 0.95,$  and  $0.96$  for  $3.7, 20$  and  $70$  mtorr, respectively. Godyak et al.<sup>17</sup> also showed  $I - V_{rf}$  data for  $3, 10, 30$  and  $100$  mtorr in a symmetric argon discharge. (Their frequency was  $13.56$  MHz; the electrode spacing was  $6.7$  cm; and the electrode material was aluminum.) At  $3$  mtorr,  $I - V_{rf}^{3/4}$  between  $10^2$  and  $10^3$  V. At  $10$  and  $30$  mtorr  $I - V_{rf}$ . At  $100$  mtorr  $I$  was roughly linear with  $V_{rf}$ , but at the highest voltages ( $V_{rf} > 500$  V) it increased slightly faster than linearly with  $V_{rf}$ . Thus, between  $10$  and  $100$  mtorr both experiments exhibit a linear  $I - V_{rf}$  relation, while at  $3.7$  mtorr our asymmetric discharge had a more linear  $I - V_{rf}$  relation. This difference may be due to the influence of electrode geometry or electrode material, which were the substantial differences between the two experiments. (For example, clean aluminum has a secondary electron emission coefficient of  $-0.1$  for  $1$  KeV argon ions compared to  $-0.7$  for copper.<sup>27</sup> Or, the enclosed geometry of the grounded electrode may better confine energetic secondary electrons, as in a hollow cathode. The role of secondary electrons will be discussed in Section IV.)

An equivalent resistance  $R$  and capacitance  $C$  can be defined from the first harmonic current and voltage amplitudes,  $I$  and  $V_{rf}$ :

$$\begin{aligned} R &\equiv \frac{V_{rf}}{I} \cos\theta \quad , \\ C &\equiv -\frac{I}{V_{rf} \omega \sin\theta} \quad . \end{aligned} \tag{1}$$

These are shown in Fig. 9.  $R$  is fairly constant with  $I$ , and shows some curvature at  $70$  mtorr. This is similar to the data of Godyak et al.<sup>17</sup> except that their data showed a larger upward curvature for each pressure between  $3$  and  $100$  mtorr over a similar voltage range. Such variation in  $R$  is observed here only for the  $70$  mtorr case. The equivalent capacitance at  $3.7, 20$  and  $70$  mtorr are fairly constant. Slightly more variation at  $3$  mtorr is seen by Godyak et al. for their symmetric discharge, but the higher pressure cases are fairly constant as in Fig. 9b.

When the power vs.  $V_{rf}$  data is plotted in logarithmic form, each curve gives close to a quadratic dependence on  $V_{rf}$ . That is,  $P - V_{rf}^n$ , where  $n \approx 1.93, 1.89$  and  $1.97$  for  $3.7, 20,$  and  $70$  mtorr, respectively. A nearly quadratic  $P - V_{rf}$  was reported by Godyak and Piejak<sup>14</sup> for  $V_{rf} > 100$  V in a symmetric  $10$  mtorr argon discharge; they found  $P - V_{rf}^{1.8}$ . Power data reported by Horwitz<sup>11</sup> also indicate a variation  $P - V_{rf}^n$ ,

where  $n \approx 1.9$  and  $1.7$ , at  $2.6$  and  $90$  mtorr, respectively. Thus, a nearly -- but slightly slower than -- quadratic variation of  $P$  with  $V_{rf}$  is not uncommon.

The phase  $\theta$  of the impedance at the first harmonic is shown in Fig. 10, and remains in the range of  $86^\circ$ - $87^\circ$  for voltages between  $100$  V and  $800$  V, at the three pressures used here. For a  $10$  MHz waveform, this amounts to a  $-0.8$  ns time shift between the two waveforms. Such a small phase shift is partly responsible for the difficulty in making accurate power measurements for low pressure rf discharges in electropositive gases. Zau et al.<sup>28</sup> have recently reported a similar conclusion in a comparative study of discharges in  $CF_4$ , Ar, and  $SF_6$ . Godyak et al.<sup>17</sup> reported data on the power factor  $\cos\theta$  for symmetric argon discharges at  $10$  and  $100$  mtorr. In the range of  $10^2$ - $10^3$  V, the phase  $\theta$  was between  $86^\circ$ - $87^\circ$  also, and showed an upward curvature similar to the  $70$  mtorr data presented here.

The discharge impedance at the second harmonic,  $Z_2$ , was obtained by fourier analyzing the current and voltage waveforms. One interesting aspect of the results is that the measured phase of  $Z_2$  is slightly greater than  $90^\circ$ , indicating inductive character at the second harmonic, but with a negative real part of the complex impedance. These results are shown in the first three columns of Table I. At all three pressures the phase of  $Z_2$  increased slightly with  $V_{rf}$ , and decreased slightly with pressure. In the fourth through sixth columns of Table I appear results from the two-sheath model of Ref. 24 for different density parameters. The seventh column gives the value of  $kT_e/e$  used in the computations. The model has been run using experimentally measured external voltage waveforms obtained at the pressure and voltage conditions listed; this is responsible for the variation of the model results with pressure. The two-sheath model assumes a uniform ion density in the sheath, and this results in an overestimate of the displacement current flowing through the sheath, when compared to a model based on a nonuniform ion density. This is compensated for by using very large density parameters; the relative size of the displacement current to the conduction current will then be reduced. The density parameter of  $23 \times 10^{10} \text{ cm}^{-3}$  in column six is meant to mimic the case of a Child law sheath with a density of  $10^{10} \text{ cm}^{-3}$  at the ion sheath edge. The model results indicate that the phase of  $Z_2$  is slightly greater than  $90^\circ$ , except for the  $-100$  V case at  $10^9 \text{ cm}^{-3}$ . The results also show a decrease in the phase with pressure. Also, upon comparing a phase at  $-100$  V and a given density parameter

with the phase at 700 V and a higher density parameter, the results show that the phase is larger in the 700V case. (Such a comparison incorporates the increase in density with voltage.) These trends are similar to the experimental data.

A phase greater than  $90^\circ$  implies that the power at the second harmonic is negative. That is, the discharge is emitting power to the external circuit. In an analytical model for power absorption in parallel plate rf discharges we found that power absorption occurs in a pulsed fashion and that electrostatic energy in the sheaths is returned to the external circuit over most of the rf cycle.<sup>29</sup> Because this analytical model assumes a sinusoidal driving current, the emitted power appears at the first harmonic. The numerical model of Ref. 24 (which we have used to obtain the results in Table I) represents a version of this same model in which the electron pulse to the electrodes is broadened. The current and voltage need not be sinusoidal either. The essential ideas remain the same, however, and the experimental results for the second harmonic power may be related to this effect when the current and voltage both contain harmonics.

#### IV. Asymmetric Discharge Model

This section presents a model for an asymmetric rf discharge. The set of equations describing the discharge is an adaptation of the symmetric discharge model of Misium et al.<sup>19</sup> The new features included are: 1) unequal sheath voltages at the two electrodes, 2) variations of the sheath edge density over the two electrodes, and 3) addition of the power carried into the discharge by secondary electrons to the electron power balance. For this study we have adopted the following simplifications: 1) the secondary electron modification of the density profile is not included (this would be important at pressures higher than  $\sim 100$  mtorr when their energy deposition is becoming localized to some small portion of the electrode spacing); 2) the two works by Lieberman<sup>30,31</sup> are used in separate models for each sheath collisionality regime, instead of unifying the treatment of collisionless and collisional sheath descriptions; and 3) this model neglects the energy carried out of the system by electrons that cross the sheath from glow to electrode.

Two conservation principles are invoked to specify the state of the discharge. The first is the particle number continuity equation for the ions,

$$u_B \sum_i A_i \langle n_{s,i} \rangle - N_0 K_i(T_e) \int dx^3 n(x) \quad (2)$$

where  $N_0$  is the neutral gas density;  $K_i(T_e)$  is the ionization rate constant (that is,  $N_0 K_i$  is the ionization frequency);  $n(x)$  is the plasma density in the glow; and  $u_B = (kT_e/M)^{1/2}$  is the Bohm speed ( $M$  is the ion mass).  $A_i \langle n_{s,i} \rangle = \int dA_i n_{s,i}(x)$ , where  $A_i$  is the area of the sheath-plasma interface above the  $i$ th electrode ( $i=PE$  or  $GE$  for the powered or grounded electrode, respectively, and we consider an electrode configuration that totally encompasses the discharge). The density at the sheath-plasma interface is  $n_{s,i}(x)$ ; that is  $n_{s,i}(x) = n(x)$  when  $x$  is on this interface. It will be shown that Eq. (2) relates the temperature  $T_e$  to the dimensions and density profile of the glow.

The second conservation principle used is energy conservation for the electrons,

$$P_{loss} = P_{ohm} + P_{st} + P_{sec} \quad (3)$$

where  $P_{loss}$  is the loss rate of electron energy to the processes of ionization, excitation, and elastic scattering;  $P_{ohm}$  is the ohmic heating of the glow electrons;  $P_{st}$  is the stochastic heating mechanism that heats glow electrons as they reflect off of the moving sheath edge; and  $P_{sec}$  represents energy deposited into the discharge by secondary electrons which are accelerated by the sheath potential. Expressions for these terms are given below:

$$P_{loss} = \sum_i E_{loss} u_B A_i \langle n_{s,i} \rangle \quad (4)$$

where  $E_{loss}(T_e)$  is the effective mean energy lost per ionization.<sup>19</sup>

$$P_{ohm} = \frac{1}{2} \frac{m_e \nu_m}{n_0 e^2} \frac{L}{A_{PE}} I^2 f_G \quad (5)$$

where  $m_e$  is the electron mass;  $e$  is the electronic charge;  $\nu_m$  is the elastic scattering frequency;  $n_0$  is the peak plasma density and  $f_G$  is a geometry factor;  $L$  is the glow length; and  $I$  is the discharge current.

$$P_{sec} = \gamma_{eff} P_{ion} = \gamma_{eff} \sum_i e V_{0,i} u_B A_i \langle n_{s,i} \rangle \quad (6)$$

where  $\gamma_{\text{eff}}$  is an effective secondary emission coefficient,  $V_{0,i}$  is the time-averaged sheath voltage, and  $P_{\text{ion}}$  is the power dissipated by ion acceleration through the sheath regions.

$P_{\text{st}}$  is discussed below in Sections A and B for the separate models of free fall or collisional ion transport through the sheaths.

In Eq. (5),  $f_G$  accounts for the nonuniform density and nonplanar geometry of the glow current density and electric field. When the electric field can be approximated as having only an axial component (as in symmetric discharges),  $f_G$  can be estimated.<sup>32,33</sup> The formula used in these computations will be discussed below once we have established a notation for the density profile. We note for now that  $f_G$  is roughly between 1.5 to 3, and varies with pressure as the density profile changes.

$P_{\text{sec}}$  is included in the electron energy balance in this model, as was also done by Godyak and Khanneh in a study of rf discharges sustained by secondary electrons,<sup>34</sup> and in Ref. 21. This treatment differs from that of Ref. 19 in which  $P_{\text{sec}}$  is included only in the expression for total power. Secondary electrons are accelerated by the sheath electric fields into the glow, and a portion of the energy they carry into the glow will go into the processes of excitation, ionization, and elastic scattering, and hence must be included in the energy balance Eq. (3). However, at these lower pressures it may be possible for a secondary electron to escape from the discharge before losing its entire energy to gas atoms. Therefore, in this model, although the secondary electron power is written  $\gamma_{\text{eff}}P_{\text{ion},i}$ , the coefficient  $\gamma_{\text{eff}}$  is really determined by both the average number of electrons emitted per ion arriving at the electrode,  $\gamma$ , and the fraction of the secondary electron energy,  $\epsilon \leq 1$ , that is deposited in the glow:  $\gamma_{\text{eff}} \equiv \epsilon \gamma$ . Also, there are several causes for electron emission from electrodes -- ion bombardment, metastable atoms, photoemission, etc. -- so that the coefficient  $\gamma_{\text{eff}}$  is not necessarily associated with a single process.<sup>35</sup> The secondary electron emission coefficient for argon ion bombardment on copper has been reported as ~0.7 at 1 KeV,<sup>36</sup> and will be less than this at lower ion energies. Thus, the ion bombardment contribution to  $\gamma_{\text{eff}}$  of a few tenths to a few hundredths (when most of the secondary electron power is lost with escaping secondary electrons) would not be unrealistic for sheath voltages in the  $10^2$  V to  $10^3$  V range.

As in previous works,<sup>21,37</sup> the discharge is described by an equivalent electrical network, with the

various components corresponding to the physical processes occurring within the discharge. Each of the components is characterized by the electron temperature, the collision frequency, the sheath voltages, and/or the discharge current. Each of the power inputs,  $P$ , in Eqs. (3) and (6) is represented by an equivalent resistance:  $R \approx 2P/I^2$ . In addition, the electrical equivalent to the glow includes an inductance  $L_g$ .<sup>38</sup>

$$\omega L_g = \frac{m_e \omega}{n_0 e^2} \frac{L}{A_{PE}} f_G \quad (7)$$

where  $\omega$  is the rf angular frequency. The displacement current through the glow has been neglected for this case where  $\omega_p^2 \gg \omega^2$  ( $\omega_p$  is the plasma frequency). Finally, the sheaths are modeled by capacitances

$$C_i = \left| I / (\omega V_{1,i}) \right| \quad (8)$$

where  $V_{1,i}$  is the first harmonic component of the sheath voltage. These electrical elements constitute a lumped circuit model for the discharge. The discharge is thus characterized by an impedance

$$Z = R_{ohm} + R_{st} + R_{sec} + R_{ion} + j \left[ \omega L_g - \sum_i 1 / (\omega C_i) \right] \quad (9)$$

where  $j^2 = -1$ . The total voltage amplitude across the two electrodes is then given by  $V_{rf} = |Z|I$ .

Lieberman and Savas<sup>39</sup> studied the dc bias that develops between the electrodes of an asymmetric rf discharge for several discharge geometries. They found ratios for the dc sheath voltages  $V_{0,i}$  by equating the total rf current flowing across the two discharge sheaths, and using a diffusion equation solution for the plasma density profile in the glow. Similar expressions for the density profile and total rf current flowing across a sheath will also be needed in Sections A and B below. The glow is modeled as a cylindrical slab of cross section  $A = \pi R^2$  and height  $L$ . A cylindrical coordinate system centered in the glow is used, so that the axial sheath edges are at  $z = \pm L/2$ . Ion motion in the glow is described by ambipolar diffusion,  $nu = -D_a \nabla n$ , where  $D_a = kT_e / (M_i \nu_i^m) = u_B \lambda_i (T_e / 3T_i)^{1/2}$  is the ambipolar diffusion constant.<sup>40</sup> Here,  $M_i$  and  $T_i$  ( $1.5kT_i \approx 0.5M_i c_i^2$ ) are the ion mass and temperature, respectively; and  $\nu_i^m$  and  $\lambda_i = c_i / \nu_i^m$  are, respectively, the total ion-neutral momentum scattering frequency and mean free path for the two processes of charge exchange and elastic scattering. Denoting the ionization frequency by  $\nu_i$ , the density profile satisfies the particle

conservation equation  $-D_a \nabla^2 n = v_i n$ , and has the form

$$n(x) = n_0 J_0(\alpha r) \cos(\beta z) , \quad (10)$$

where  $J_0$  is the zero order Bessel function of the first kind. The coefficients  $\alpha$  and  $\beta$  are determined by setting the ion flow speed at the sheath edge to the Bohm speed, or equivalently by requiring  $-D_a \nabla n = n_s u_B$  at the sheath edge. When this condition is evaluated at  $x = (r, z) = (0, \pm L/2)$ ,  $b = \beta L/2$  is given by

$$(L u_B)/(2 D_a) \cos(b) - b \sin(b) = 0 . \quad (11)$$

And when the boundary condition is evaluated at  $x = (R, 0)$ ,  $a = \alpha R$  is given by

$$R (u_B/D_a) J_0(a) - a J_1(a) = 0 . \quad (12)$$

where  $J_1$  is a Bessel function. The short mean free path limit was used in Ref. 39 and this gave  $\alpha = \chi_{01}/R$  ( $\chi_{01} = 2.405$  is the first zero of  $J_0$ ), and  $\beta = \pi/L$ . However,  $\alpha$  and  $\beta$  can be considerably smaller than these values at the pressures and cavity dimensions used in the experiment. This is shown by the values for  $a$  and  $b$  listed in Table II.

There are limits to the values for  $\alpha$  and  $\beta$ . First, presheath electric fields in the collisionless ion motion regime will give a minimum electron density attenuation from the center of the glow to the sheath edge. This idea was used in Ref. 19 to set an upper bound for  $n_s(x)/n_0$  of  $e^{-1/2} = 0.606$  at very low pressures. This implies lower bounds on  $\alpha R$  and  $\beta L/2$  of  $-1.32$  and  $-0.92$ , respectively, and these values were substituted for  $a$  and  $b$  when Eqs. (11) and (12) gave values below these lower bounds.

Secondly, an upper limit should exist on  $\alpha R$  for pressures greater than a few tens of millitorr. For example, localized ohmic heating near the sheath edge can increase the sheath edge density above that implied by  $\alpha$  and  $\beta$  of Eqs. (11) and (12) when the discharge is very collisional and the electron thermal conductivity is poor. Godyak and Ganna studied this theoretically and experimentally, and presented data for a helium rf discharge showing that the ratio of the plasma density at the sheath edge to that at the center of the glow varied from  $\sim 0.4$  to  $\sim 0.2$  with increasing pressure between 0.1 and 1 torr.<sup>40</sup> They also gave a condition for which their mathematical model was valid:  $(2T_e \lambda_i)/(T_i L) \ll 1$ . In our experiment, this condition is closer to equality, but this probably means that the heating is not entirely localized. Additionally, their data suggests

that the density ratios are above -0.1 over a wide pressure range. Thus, taking this figure as an estimated lower bound for the density ratio, this gives a maximum  $\alpha R \approx 2.2$ . (The corresponding upper limit for  $\beta L/2$  is -1.5. This, however, is not encountered in our experiment.)

Estimates for the density at the sheath edge are now obtained from Eq. (10). Along the sheath boundaries at  $z = \pm L/2$ ,  $n_s(x)$  is approximated by

$$n_s(r, \pm L/2) = n_s(0) J_0(\alpha r) , \quad (13)$$

where  $n_s(0) = n_0 \cos(b)$ . Along the sheath edge at  $r=R$ ,

$$n_s(R, z) = n_s(0) \left( J_0(\alpha R) / \cos(\beta L/2) \right) \cos(\beta z) . \quad (14)$$

The boundary conditions Eqs. (11) and (12) can be used to show

$$\frac{J_0(a)}{\cos(b)} = \frac{L}{2R} \frac{a J_1(a)}{b \sin(b)} , \quad (15)$$

so that along the radial boundary

$$n_s(R, z) = n_s(0) \frac{L}{2R} \frac{a J_1(a)}{b \sin(b)} \cos(\beta z) . \quad (16)$$

Expressions for the volume and surface integrals in Eqs. (2) - (6) are derived from the density profiles in Eqs. (10), (13), and (16). One obtains

$$\int d^3x n(x) = n_0 (\pi R^2 L) \frac{2J_1(a)}{a} \frac{\sin(b)}{b} , \quad (17)$$

$$A_{PE} \langle n_{s, PE} \rangle = n_s(0) \pi R^2 \frac{2J_1(a)}{a} , \quad (18)$$

and

$$A_{GE} \langle n_{s, GE} \rangle = n_s(0) \pi R^2 \frac{2J_1(a)}{a} \left[ 1 + \frac{1}{2} \left( \frac{aL}{bR} \right)^2 \right] . \quad (19)$$

Equation (2) can be rewritten

$$\frac{2u_B(T_e)}{K_i(T_e)} = N_0 L \frac{\tan(b)}{b} \left[ 1 + \left( \frac{aL}{2bR} \right)^2 \right]^{-1} \equiv N_0 L_{eff} . \quad (20)$$

Equation (20) gives  $T_e$  for a given value of  $N_0 L_{eff}$ . This determines the elastic scattering frequency  $\nu_m = N_0 K_m(T_e)$  and the mean energy loss per ionization,  $E_{loss}(T_e)$ , for a maxwellian energy distribution. The solution  $T_e(N_0 L_{eff})$  and the other functions of  $T_e$  were computed by Misium et al.,<sup>19,41</sup> and Table II lists the values of  $T_e$ ,  $E_{loss}$ , and  $K_m$  found as a consistent set in the computations. The variables  $a \equiv \alpha R$  and  $b \equiv \beta L/2$  depend on  $T_e$  through  $D_a$ . In order to simplify the computations and make use of the numerical results of Ref. 41,  $L_{eff}$  was computed assuming  $kT_e = 3eV$  (and  $kT_i = 0.025 eV$ ). This  $T_e$  is close to the  $T_e$  shown in Table II, and in practice there are also uncertainties in  $T_i$  and  $\lambda_i$  which enter. Hence, this was a reasonable simplification to adopt for the computations.

Having established a notation for the density profile, the formula for  $f_G$  in the ohmic power, Eq. (5), will now be given. The modification of the glow impedance due to a nonuniform glow density is estimated by borrowing a result from the simpler case where current flows strictly in the axial direction. Consider a cylindrical slab glow of radius  $R$  and height  $L$ , where the current density flows along the  $z$  direction and the density is of the form  $n(x) = n_0 K_z(z) K_r(r)$ , as in Eq. (10). The glow impedance has the form<sup>32</sup>

$$Z_{glow} = Z_u \frac{\langle K_z^{-1} \rangle}{\langle K_r \rangle} \quad (21)$$

where  $Z_u$  is the glow impedance for a uniform density glow and

$$\begin{aligned} \langle K_z^{-1} \rangle &= \frac{1}{L} \int dz \frac{1}{K_z(z)} , \\ \langle K_r \rangle &= \frac{1}{\pi R^2} \int dr 2\pi r K_r(r) , \end{aligned} \quad (22)$$

where the integrals are over the respective dimensions of the glow. Thus, the geometry factor  $f_G$  is  $(K_z^{-1})/(K_r)$ . Approximating  $J_0(aR)$  and  $\cos(\beta z)$  with parabolic expressions having the same density ratios  $h_r = n(R,0)/n_0 = J_0(a)$  and  $h_z = n(0,L/2)/n_0 = \cos(b)$ ,  $f_G$  is given by

$$f_G = \left[ (1 + h_r)(1 - h_z)^{1/2} \right]^{-1} \ln \left\{ \frac{1 + (1 - h_z)^{1/2}}{1 - (1 - h_z)^{1/2}} \right\} . \quad (23)$$

Values for  $f_G$  used at each pressure are given in Table II.

The correction factor  $f_G$  for the cylindrical slab glow with a nonuniform plasma density and radial components to the current density requires solution of Poisson's equation. The effect of radial components of the current density can be studied with the example of a rectangular cavity filled with a homogeneous dielectric, with one end wall of the cavity (the powered electrode) held at some potential difference with respect to the remaining walls of the cavity (the grounded electrode). Our problem reduces to finding how the capacitance for this geometry differs from the simple one-dimensional result. Let the cavity be of length A, width B, and height C, and let the powered electrode be the bottom side of this box. A gap of width d around the edge of the powered electrode must be included in the boundary conditions to avoid infinite fields at the electrode edges. For simplicity we assume a linear decrease of the potential in this gap. One can show that the capacitance  $C_{box}$  is

$$C_{box} = \epsilon_0 \frac{AB}{C} \frac{4^3}{\pi^4} \sum_{ij} \frac{1}{(ij)^2} \frac{k_z C}{\tanh(k_z C)} \frac{\sin(2k_x d) \sin(2k_y d)}{(2k_x d)(2k_y d)} \quad (24)$$

$$\approx \epsilon_0 \frac{AB}{C} \frac{1}{f_G} ,$$

where  $i,j = 1, 3, 5, \dots$ ;  $k_x = \pi i/A$ ,  $k_y = \pi j/B$ , and  $k_z^2 = k_x^2 + k_y^2$ . The factor  $f_G$  is then between 0.5 and 1 for gap sizes of 2 to 4 mm, when the cavity height is chosen as 2.5 inches and the length of both sides is 9 inches. Because the side walls of the ground electrode are closer to the powered electrode, the impedance between the two decreases. We refrain from explicitly including this correction due to uncertainty in its magnitude, and the effects of nonuniform plasma conductivity. However, varying  $f_G$  over a range of 1.5 to 3 for all pressures studied here did not result in significant changes in the results. This is because ohmic heating (where  $f_G$  appears) is not the major electron power input at the pressures used in the experiment.

## A. Collisionless Sheaths

In this section the stochastic heating power for the collisionless sheath is introduced and is used with the foregoing results to form the collisionless sheath discharge model.

The collisionless sheath model of Ref. 30 gives formulae for the sheath voltage and the sheath conductance associated with stochastic heating. In the present model, these relations are assumed to hold locally, but variations across an electrode are allowed. This is adequate when the scale length for density variation along an electrode is much larger than the sheath thickness. The total admittance of a sheath is then obtained by integrating the admittance per unit area over an entire electrode. The sheath voltage is nearly uniform over a given sheath; the electric potential in the glow can vary only by a few  $kT_e/e$ , so that for sheath voltages much larger than this, the properties of the sheath at different points along an electrode can be described satisfactorily by a uniform sheath voltage. The time-averaged sheath voltage  $V_{0,i}$  is given in Ref. 30 as

$$V_{0,i} = \frac{\pi}{4} \frac{kT_e}{e} H_i \left( 3 + \frac{9\pi}{8} H_i \right) , \quad (25)$$

where  $H_i$  is given in terms of the rf current density  $J_i(x)$  over the  $i$ th electrode as

$$H_i = J_i^2(x) / \left( \pi \omega^2 \epsilon_0 kT_e n_{s,i}(x) \right) . \quad (26)$$

Thus, if the glow is a dc equipotential, then  $H$  -- or  $J^2/n_s$  -- is also constant over a sheath. Ref. 30 also shows that the rf voltage in a sheath is also expressible in terms of  $H$ , so that the glow is an rf equipotential once it is assumed to be a dc equipotential.

Current continuity through the discharge yields a relation between the sheath voltages at the two electrodes. This problem was studied in Ref. 39 where the result for the collisionless sheath was developed for the case where  $H_i \gg 1$  so that  $V_{0,i}$  in Eq. (25) is proportional to  $H_i^2$ . For smaller values of  $V_{0,i}$  (for example, the larger area sheath of an asymmetric system) this is less accurate, and the correction is not difficult to do. It is useful to define two functions  $f_i(x)$ ,  $i=PE$  or  $GE$ , which define the density profile along a sheath edge:

$$n_{s,i}(x) = n_s(0) f_i(x) \quad . \quad (27)$$

The density profile functions are given explicitly through Eqs. (13) and (16). Eq. (26) can be solved for  $J_i(x)$  of the form  $J_i(x) = J_i(0) f_i^{1/2}(x)$ , and this can be integrated over the electrode to obtain the discharge current

I. Equating two such equations give a relation between the  $H_i$ :

$$\frac{H_{PE}}{H_{GE}} = \left[ \frac{A_{GE} \langle f_{GE}^{1/2} \rangle}{A_{PE} \langle f_{PE}^{1/2} \rangle} \right]^2 \quad . \quad (28)$$

Expressions for the integrals  $A_i \langle f_i^p \rangle$  are listed below. Similar integrals --  $\langle f_i^{2/5} \rangle$  -- will be required for the collisional sheath model. We have:

$$A_{PE} \langle f_{PE}^p \rangle = 2\pi R^2 \left( \frac{\chi_{01}}{a} \right)^2 G_p \left( \frac{a}{\chi_{01}} \right) \quad (29)$$

$$A_{GE} \langle f_{GE}^p \rangle = 2\pi R^2 \left\{ \left( \frac{\chi_{01}}{a} \right)^2 G_p \left( \frac{a}{\chi_{01}} \right) + \left( \frac{L}{R} \right)^{(1+p)} \left[ \frac{a J_1(a)}{2b \sin(b)} \right]^p \left( \frac{\pi}{2b} \right) F_p \left( \frac{2b}{\pi} \right) \right\} \quad . \quad (30)$$

( $\chi_{01}$  is the first root of the zero order Bessel function  $J_0$ .) The functions  $G_p$  and  $F_p$  are defined by

$$\begin{aligned} G_p(y) &= \int_0^y du u \left[ J_0(\chi_{01} u) \right]^p \\ F_p(y) &= \int_0^y du \left[ \cos \left( \frac{\pi}{2} u \right) \right]^p \end{aligned} \quad (31)$$

for  $0 \leq y \leq 1$ .<sup>39</sup> Table II presents the values of  $G_p$  and  $F_p$  used in the computations.

$P_{ohm}$  in Eq. (5) is proportional to  $I^2/n_0$ . This suggests expressing  $P_{ohm}$  in terms of  $H_{PE}$ . Using the definition of  $J_{PE}(x)$  and Eq. (26), one finds

$$\frac{I^2}{n_0} = H_{PE} \pi \omega^2 \epsilon_0 k T_e \left( A_{PE} \langle f_{PE}^{1/2} \rangle \right)^2 \cos(b) \quad . \quad (32)$$

Thus,  $P_{ohm}$  can be expressed in terms of  $H_{PE}$  with no explicit dependence on  $n_s(0)$ .

The stochastic heating per unit area given in Ref. 30 yields

$$P_{st} = \sum_i \frac{3\pi^2}{32} (\epsilon_0 m_e \omega^2 c_e k T_e / e^2) H_i^2 A_i \quad (33)$$

when integrated over both electrodes. Thus  $P_{st}$  can also be expressed in terms of the  $H_i$ 's, with no explicit dependence on  $n_s(0)$ .

Equation (4) shows that  $P_{loss}$  is proportional to  $n_s(0)$ , and Eq. (6) shows that  $P_{sec}$  is also proportional to  $n_s(0)$ , and depends on a quadratic expression in  $H_i$  through  $V_{0,i}$ . These expressions for  $P_{ohm}$ ,  $P_{st}$ ,  $P_{sec}$  and  $P_{loss}$ , when inserted into Eq. (3), give a relation between the  $H_i$  and  $n_s(0)$ . For notational purposes, let us define  $g_{loss}$  and  $g_{sec}$  by  $P_{loss} \equiv g_{loss} n_s(0)$  and  $P_{sec} \equiv g_{sec} n_s(0)$ . Then  $n_s(0)$  is given by

$$n_s(0) = (P_{ohm} + P_{st}) / (g_{loss} - g_{sec}) \quad (34)$$

Note that the denominator arises from the difference in the secondary electron power and the electron energy loss term  $P_{loss}$ : a divergence in  $n_s(0)$  occurs when the discharge is being sustained solely by the secondary electron power. This will be discussed further in Section VI.

A final constraint on the solution is that the total length of the glow and the sheaths is the cavity height  $D$ . This is included in a more limited manner as a constraint on the sheath thicknesses on axis (at  $r=0$ ):

$$\sum_i s_{m,i}(0) + L = D \quad (35)$$

where the maximum sheath thickness  $s_{m,i}$  is given in Ref. 30:

$$s_{m,i} = \lambda_D (\pi H_i)^{1/2} \left( 2 + \frac{5\pi}{12} H_i \right) \quad (36)$$

where  $\lambda_D$  is the Debye length  $(\epsilon_0 k T_e / n_s e^2)^{1/2}$ .

Equations (2), (28), (34), (35), and (36) form a set of constraints on the six variables  $L$ ,  $T_e$ ,  $H_{GE}$ ,  $n_s(0)$ , and  $s_{m,i}$  ( $i=PE$  or  $GE$ ).  $H_{PE}$  is considered independent. The values of these parameters can then be used to find other quantities in the discharge model. In particular, Eq. (32) may be used to obtain the discharge current, which in turn may be used to obtain  $C_i$  (Eq. (8)), with  $V_{1,i}$  given in Ref. 30 as

$$V_{1,i} = \frac{\pi}{2} \frac{k T_e}{e} H_i (2 + 2.14 H_i) , \quad (37)$$

To simplify the numerical search for a solution to the set of equations (2), (34), (28), (35), and (36), the radius of the glow,  $R$ , was not adjusted at each voltage. The sheath thickness at the grounded electrode did not change drastically with voltage so that it was possible to use a fixed value of  $R$ . This was chosen so that the sum of the glow radius  $R$  and the sheath thickness at  $x = (R,0)$  was close to the 11.4 cm cavity radius. Variation in this total radius, with this computational simplification, was only a few millimeters. Thus, this simplification did not significantly affect the results.

## B. Collisional Sheaths

In this section we examine the stochastic heating power in the collisional sheath regime, and the formulation of the electron power balance in terms of  $n_s(0)$  and  $I$ .

Ref. 31 gives formulae for the sheath voltage and the stochastic power per unit area of electrode when the mean free path for symmetric charge exchange is much smaller than the sheath thickness. The time-averaged sheath voltage can be written in terms of the rf current density  $J_i(x)$  and  $n_{s,i}(x)$  at the  $i$ th electrode:

$$V_{0,i} = \left[ \frac{2\lambda_i}{\pi^2 \epsilon_0^3 e k T_e \omega^5} \right]^{1/2} \frac{J_i^{5/2}(x)}{n_{s,i}(x)} , \quad (38)$$

where  $\epsilon_0$  is the permittivity of free space. In this case,  $J^{5/2}/n_s$  is constant over the lateral extent of a sheath, and thus the current density may be expressed in terms of the density profile function as  $J_i(x) = J_i(0) f_i^{2/5}(x)$ , where  $J_i(0)$  is the current density at  $x = (0, \pm L/2)$ .  $J_i(0)$  can be related to the discharge current  $I$  by integrating  $J_i(x)$  over the  $i$ th electrode.  $V_{0,i}$  can then be expressed in terms of  $I$  and  $n_s(0)$  by evaluating Eq. (38) at  $x = (0, \pm L/2)$ :

$$V_{0,i} = \left[ \frac{2\lambda_i}{\pi^2 \epsilon_0^3 e k T_e \omega^5} \right]^{1/2} \frac{1}{n_s(0)} \left( \frac{I}{A_i f_i^{2/5}} \right)^{5/2}, \quad (39)$$

where the average over  $f_i^{2/5}$  is given in Eqs. (29) and (30).

The stochastic heating term given in Ref. 31 can be written as

$$P_{st} = \sum_i \left( \frac{\epsilon_0 m_e \omega^2 c_e}{2.04 e} \right) V_{0,i} A_i, \quad (40)$$

and depends explicitly on the sheath voltage. It is more convenient to express the electron energy conservation in terms of  $n_s(0)$  and  $I$ , instead of  $n_s(0)$  and  $V_{0,i}$  (or  $H_i$ ) as was done in the collisionless sheath model. Equation (39) is used to replace  $V_{0,i}$  with  $I$  and  $n_s(0)$ .  $P_{st}$  is then proportional to  $I^{5/2}/n_s(0)$ .

Equation (39) also shows that the product of  $n_s(0)V_{0,i}$  is proportional to  $I^{5/2}$ , and this can be used to express  $P_{ion}$  (see Eq. (6)) strictly in terms of  $I$ . The electron energy balance equation can now be expressed in terms of  $n_s(0)$  and the discharge current  $I$ . Defining  $g_{loss}$ ,  $g_{ohm}$ , and  $g_{st}$  by  $P_{loss} \equiv g_{loss} n_s(0)$ ,  $P_{ohm} \equiv g_{ohm}/n_s(0)$ , and  $P_{st} \equiv g_{st}/n_s(0)$ , electron energy balance can be solved for  $n_s(0)$ :

$$n_s(0) = \frac{P_{sec}}{2g_{loss}} + \left[ \left( \frac{P_{sec}}{2g_{loss}} \right)^2 + \frac{g_{ohm} + g_{sec}}{g_{loss}} \right]^{1/2}. \quad (41)$$

The discharge length constraint, Eq. (35), also applies here. Ref. 31 gives the result for the maximum sheath thickness; on axis, at  $x=(0, \pm L/2)$ , the sheath thicknesses are

$$s_{m,i}(0) = 1.95 \left[ \frac{2\lambda_i}{\tau^2 \epsilon_0 e k T_e \omega^3} \right]^{1/2} \frac{1}{n_s(0)} \left[ \frac{I}{A_i \langle f_i^{2/5} \rangle} \right]^{5/2} . \quad (42)$$

Equations (2), (35), (41), and (42) are constraints on the variables  $T_e$ ,  $L$ ,  $n_s(0)$ , and  $s_{m,i}$  ( $i=PE$  or  $GE$ ). (The discharge current  $I$  is the independent variable.) Other discharge quantities may be calculated once a consistent set of these parameters is known. In particular, the sheath capacitances  $C_i$  are obtained from Eq. (8) using the result from Ref. 31 for  $V_{1,i}$ :

$$V_{1,i} = 1.28 V_{0,i} . \quad (43)$$

The numerical search for a consistent set of  $T_e$ ,  $L$ ,  $n_s(0)$ , and  $s_{m,i}$  was simplified by using a fixed value for  $R$ , the glow radius, as described in the collisionless sheath model.

The collisional sheath model developed in Ref. 31 gives the ions the Bohm speed at the sheath edge. Godyak<sup>42</sup> showed, in a fluid description of the sheath edge, that the ion speed is reduced below the Bohm speed by a factor of  $(1 + (\tau\lambda_D)/(2\lambda_{cx}))^{1/2}$  when the frictional force on the ions is due to charge exchange collisions ( $\lambda_{cx}$  is the mean free path for charge exchange). In argon at 70 mtorr, this factor is -1.18, upon taking  $kT_e \approx 2$  eV,  $n_s \approx 5 \times 10^9$  cm<sup>-3</sup>, and  $\lambda_{cx} \approx 0.06$  cm. At lower pressures, this factor is even closer to unity. Thus, for the pressures used in the experiment, the model of Ref. 31 suffices. At higher pressures this correction to the ion speed at the sheath edge should be included. Then, however, the present model becomes limited by other pressure dependent effects; these will be discussed later.

## V. Model Results and Discussion

The results of the foregoing models are plotted with experimental data in Figs. 5 - 7. The results from the collisionless sheath model are shown in Fig. 5 for the 3.7 mtorr case; the results of the collisional sheath model are shown in Fig. 7 for the 70 mtorr case; and the results of both models are shown in Fig. 6 for the 20 mtorr case. Table III presents a comparison of the ion mean free path used in the computations to the values of the maximum sheath thickness, on axis, at the powered and grounded electrodes. The 20 mtorr case is marginally a mixture of ion transport regimes, with the powered electrode sheath being three or more mean

free paths thick and the grounded electrode sheath being one or more mean free paths thick. For this reason, the results for both sheath models are presented for the 20 mtorr case. Curves for no secondary emission ( $\gamma_{\text{eff}} = 0$ ) and for some  $\gamma_{\text{eff}} > 0$  appear for each pressure. Each such curve is labeled by the value of  $\gamma_{\text{eff}}$ .

There are two parameters that enter into the computations. The first is the effective secondary emission coefficient and the second is the mean free path. The mean free path is  $\lambda_i = C_1/p$ , where  $p$  is the pressure in millitorr, and  $C_1$  is a constant. The results shown are for  $C_1 \approx 0.039$  (when  $\lambda_i$  is in meters), as suggested by data from McDaniel.<sup>43</sup> The models have also been run for  $C_1$  up to 0.08, and in all cases varying  $C_1$  over this range caused only a modest change in the current and power results which could be compensated by adjustments in  $\gamma_{\text{eff}}$  of less than 20%. Thus, in practical terms, only adjustments in  $\gamma_{\text{eff}}$  give large changes in the results, and hence only  $\gamma_{\text{eff}}$  is a useful fitting parameter.

We note that the fit of the models to the current data does not automatically imply a fit of the model results to the experimental power data. The total power is given largely by the power at the first harmonic  $P = 0.5 I V \cos \theta$ , where  $\theta$  is the phase shift between the first harmonic current and voltage. Thus, the phase shift must be reproduced by the model, independent of the fit to the current data, if the power results are to match the experimental data.

#### A. The DC Bias

The model results for the dc bias  $V_{\text{dc}} \equiv V_{0,\text{pe}} - V_{0,\text{ge}}$  are shown in Figs. 5a, 6a, and 7a. The model  $V_{\text{dc}}$  results linearly extrapolate to zero. This is because the floating electrode constraint was not explicitly included in Ref. 30 and 31. As mentioned in Section III, this condition gives  $V_{\text{dc}}$  a quadratic dependence on  $V_{\text{rf}}$  for small rf voltages.

The dc bias graphs show some disagreement in the slopes of  $V_{\text{dc}}$  vs.  $V_{\text{rf}}$ . Table IV gives the slopes of the experimental and model results when each is fitted to a line. The collisional sheath model gives the closest agreement, with the experimental slopes being larger by -16%. The sheath thicknesses given by the model in these cases were 0.83 cm or less (see Table III). The 3.7 mtorr case shows the largest difference between the experimental data and the collisionless sheath model result; the experimental slope is -34%

smaller than the model result. The sheath thicknesses given by the model in this case were roughly a factor of two larger than at 20 mtorr, and consequently the approximation of the glow as a cylindrical slab may be less accurate for purposes of computing the glow volume and sheath area integrals.

The slope of the dc bias vs. rf voltage was more sensitive to the mean free path  $\lambda_i$  than either the discharge current  $I$  or the total power  $P_{tot}$ . If the mean free path parameter  $C_1$  is increased by a factor of two, the agreement between the experiment and model for  $I$  and  $P_{tot}$  could be maintained, and the slope of the dc bias could also be made to agree. Thus, the dc bias was sensitive to the density profile through the value of the integrals  $A_i \langle f_i^{1/2} \rangle$ . This suggests again that disagreement in the slope of  $V_{dc}$  vs.  $V_{rf}$  is partly due to the approximations taken to compute these area integrals. Since the fourth power of the ratio  $(A_{ge} \langle f_{ge}^{1/2} \rangle) / (A_{pe} \langle f_{pe}^{1/2} \rangle)$  is involved, modest errors in this ratio yield larger errors in the slope of  $V_{dc}$  vs.  $V_{rf}$ . For example, in the limit that  $H_{pE}$  and  $H_{GE}$  are much greater than unity, an 11% error in this ratio yields the 34% discrepancy in the slope of  $V_{dc}$  vs.  $V_{rf}$  noted in Table IV.

Part of the disagreement in the slope of  $V_{dc}$  vs.  $V_{rf}$  can also be due to the omission of the floating electrode constraint. Godyak and Sternberg<sup>44</sup> recently studied a sheath model that included this condition, and found that the dc sheath voltage  $V_{0,i}$  can still be -10% greater than the expressions used here even for voltages  $eV_{1,i}/(kT_e)$  as large as ~ 500. Thus, the expressions for  $V_{0,i}$  used here involve some inaccuracy; but it is not simple to use the results of Ref. 44 and apply them immediately to an asymmetric discharge to discover the dc bias. However, one can see that there is an inconsistency in the dc bias in the limit of a very asymmetric discharge (the "single sheath" limit). In this limit  $V_{1,ge} \approx V_{0,ge} \approx 0$  for the model discussed here, and hence,

$$\frac{V_{dc}}{V_{rf}} = \frac{V_{0,pe}}{V_{1,pe}} \quad (44)$$

(At the pressures of interest, the rf voltage across the glow is negligible in comparison to  $V_{1,pe}$ , and has been omitted from the denominator.) For large rf voltages this gives  $V_{dc}/V_{rf} \approx 0.83$  and  $0.78$  for the collisionless and collisional sheath models, respectively. In comparison, graphical results in Fig. 8 of Ref. 44 indicate this ratio should be closer to unity. Additionally, the experiment is closer to a discharge driven by a sinusoidal

voltage (not current), and for such a discharge  $eV_{dc}/kT_e = \ln(I_0(eV_{rf}/kT_e))$  in the infinite area ratio limit. For example, if  $eV_{rf}/kT_e = 100$ , then  $eV_{dc}/kT_e \approx 96.8$ , and the ratio  $V_{dc}/V_{rf}$  would be larger than the -0.8 given above. In the single sheath limit the expressions for  $V_{0,i}$  and  $V_{1,i}$  used here give  $V_{dc}/V_{rf}$  ratios that are too small, and this may extend to the 20 mtorr and 70 mtorr cases for which the model's slope was slightly low. The 3.7 mtorr case is quite different, and this may indicate that glow geometry considerations are more important for this case.

## B. The RF Impedance

Figure 5b shows the rf current at 3.7 mtorr for  $\gamma_{eff} = 0$  and 0.03. The experimental data is fairly linear, but the  $\gamma_{eff} = 0$  curve is rootlike. If only the stochastic power were present, the model gives a scaling of  $I \propto V_{rf}^{3/4}$  at large  $V_{rf}$ . In this case, the sheath thickness grows with  $V_{rf}$ , resulting in a decreasing sheath capacitance and sheath admittance; thus the current should rise sublinearly with voltage. Adding the power deposited by secondary electrons causes an increase in the plasma density (for a given rf voltage) and this slows the increase in the sheath thickness. This is illustrated in Fig. 11 which shows the variation of the sheath thickness with voltage for the 3.7 mtorr case with no secondary electron power, and when a  $\gamma_{eff} = 0.03$  is used. An even greater effect is also observed for the larger  $\gamma_{eff}$  used in collisional sheath model cases. The sheath impedance  $1/(\omega C) \propto s_m$  increases more slowly when secondary electrons are included, and hence the I-V characteristic is closer to that of a linear element.

The value of  $\gamma_{eff}$  was chosen to replicate the fairly linear rise in I with V. Using this  $\gamma_{eff}$ , the model yields a value for the total power  $P_{tot} \approx P_{ion} + P_{loss}$ , shown in Fig. 5c. The curves for both  $\gamma_{eff} = 0$  and 0.03 are close to the experimental power data. At  $\gamma_{eff} = 0.02$  (not shown) the model curve matches the experimental data at 700V, but the linearity of I with V is sacrificed somewhat at this smaller  $\gamma_{eff}$ .

The collisional sheath model results for the 70 mtorr argon discharge are given in Fig. 7. The current is given in Fig. 7b for  $\gamma_{eff} = 0$  and 0.16. With no secondary electron power, the current varies sublinearly with  $V_{rf}$ . If stochastic heating were the dominant mechanism for electron energy absorption, then the rf current I would vary as  $V_{rf}^{4/5}$ . At this pressure however, ohmic heating is significant, though always less than  $P_{st}$  for

$V_{rf} > 100$  V. Thus the behavior of  $I$  is a mixture of the two contributions:  $V_{rf}^{4/5}$  from  $P_{st}$ , and  $V_{rf}^{2/3}$  from  $P_{ohm}$ . As in the 3.7 mtorr case, including a secondary electron power term in the electron energy balance increases the plasma density and inhibits increases in the sheath thickness and the sheath impedance. This then brings the variation of  $I$  with  $V$  closer to a linear dependence.

The model results for the total power  $P_{tot}$  are shown in Fig. 7c. The  $\gamma_{eff} = 0$  curve is -20-30% lower than the experimental data, but comparison between the  $\gamma_{eff} = 0$  and 0.16 curves shows the importance of including this extra energy deposition mechanism in the electron energy balance.

The model results for the 20 mtorr argon discharge appear in Fig. 6. Figure 6b shows the current for both collisionless and collisional sheath models. The collisional sheath results match the experimental data much better. A value of  $\gamma_{eff} = 0.08$  is sufficient to stabilize the sheath thickness growth at large voltage and maintain a linear relationship between  $I$  and  $V$ . Additionally, this value of  $\gamma_{eff}$  simultaneously gives a good match in the power results shown in Fig. 6c. The collisionless sheath model results also appear in Figs. 6b and 6c. One finds that a larger value of  $\gamma_{eff}$  -- 0.125 -- is required in the collisionless sheath model to bring the power result (Fig. 6c) up to the experimental data at 700 V, and even this value for  $\gamma_{eff}$  cannot increase the slower variation of  $I$  shown in Fig. 6b by the curve labeled "free fall." Thus, although mean free path considerations do not imply highly collisional ion transport through the sheath, the results indicate remarkable agreement between the collisional sheath model and the experimental data.

Figures 5 - 7 show that secondary electron power deposition can affect the discharge current and power. For  $V_{rf} > 400$  V the electron powers are only a small part of the total discharge power. The discharge power at these voltages is dominated by  $P_{ion}$  since the energy associated with each lost ion,  $eV_{0,i}$ , is several times the energy associated with each lost electron,  $E_{loss}$ . An example of this is shown in Fig. 12a which compares  $P_{ion}$  with  $P_{st}$  (for reference) for the 20 mtorr collisional model result. Figure 12b shows the corresponding electron power terms  $P_{st}$ ,  $P_{sec}$  and  $P_{ohm}$ . Similar results hold for the 3.7 mtorr and 70 mtorr cases; namely, at 400 V the ion power is ~4 times the stochastic heating power, and at 800 V this ratio is significantly greater. Figures 6 and 7 show, however, that addition of the secondary electron power can increase the total power by a factor of almost 2 or more at 800 V. It is notable that the addition of a

seemingly small power contribution can increase the total power by such a large amount. The reason is that while secondary electron power is a small fraction of the total power, it can be a significant fraction of the total electron power, and hence can significantly affect the plasma density. The total power will then increase since more ions will be accelerated across the sheaths. The different contributions to the total electron power are shown in Figs. 12b (20 mtorr case) and 13 (3.7 and 70 mtorr cases). At 3.7 mtorr  $P_{st}$  dominates the electron power, although  $P_{sec}$  is becoming appreciable at large voltages. At 20 mtorr  $P_{sec}$  is comparable to  $P_{st}$  above -400 V; and at 70 mtorr  $P_{sec}$  becomes the largest electron power deposition mechanism for  $V_{rf} > 500$  V. The enhanced plasma density resulting from secondary electron power is responsible for reducing (or even reversing) the growth in sheath thickness (thus giving a more linear  $I - V_{rf}$ ) and increasing the total discharge power.

## VI. Discussion

### A. Secondary Electrons

In this model the effect of properly including secondary electron power in the electron power balance was seen to improve the linearity of the dependence of  $I$  on  $V_{rf}$ . Secondary electron power also improved the agreement of the experimental and model values for the total discharge power, even though the fit of the current data does not guarantee a fit of the power data. These results are an improvement over the model of Misium et al.<sup>19</sup> which gave a sublinear  $I - V_{rf}$  relations and too small a power at large  $V_{rf}$ .<sup>45</sup>

The improved agreement between the model results and experimental data is interesting in light of other attempts to explain the linear  $I - V_{rf}$  relation. Surendra and Graves<sup>46</sup> performed particle-in-cell (PIC) simulations for (symmetric) helium discharges at 250 mtorr and 12 or 30 MHz. They showed that  $I$  was proportional to  $V_{rf}$  even without secondary electrons. Similar preliminary results have recently been produced by Mirrashidi et al.<sup>47</sup> for argon discharges at 3 and 10 mtorr. (Kushner<sup>48</sup> also studied electron power deposition using a Monte Carlo simulation and claimed that secondary electrons were not significant. His conditions, however, were for rf sheath voltages  $V_{1,i}$  in the 75 to 125 V range, and his claim is consistent with the low voltage results of the present model.)

Godyak and Sternberg<sup>44</sup> showed that careful treatment of ion collisionality in the sheath and inclusion of the floating electrode constraint in a sheath model could give a fairly linear  $I$  vs.  $V_{rf}$  if  $T_e n_s / J$  remained constant with  $I$ . This implies that an additional mechanism like secondary electron power is unnecessary. However, in the absolutely collisionless limit, the sheath model of Ref. 44 produces a sublinear  $I$  vs.  $V_{rf}$  (if  $T_e n_s / J$  remains constant). Their model is sensitive to the degree of collisionality at very small collisionality, and requires some collisionality to give a linear  $I$  vs.  $V_{rf}$ .

In contrast, Godyak et al.<sup>17</sup> presented data for a symmetric argon discharge that showed a superlinear  $I$  vs.  $V_{rf}$  for large  $V_{rf}$  at pressures above 0.1 torr. This could be interpreted in terms of an additional power mechanism which has the effect of decreasing the sheath impedances preferentially at large  $V_{rf}$ .

Additionally, Bletzinger<sup>49</sup> reports experiments in argon discharges in which the discharge impedance increased by -5 - 10% at 0.1 torr when the cathode surface was changed from aluminum to a coating of Aquadag, which has a  $\gamma$  that is roughly half of that of aluminum.  $V_{rf}$  was -40 V in these experiments. This shows that, at least at 0.1 torr, secondary electrons do influence the discharge current to some extent. Also, Surendra et al.<sup>50</sup> reported a -10% increase in the plasma density when secondary electrons were included in PIC simulations for a 60 mtorr helium discharge. The secondary emission coefficient used was 0.1, the rf frequency was 30 MHz, and  $V_{rf}$  was 800 V in their simulation. Thus, it is probably incorrect to neglect the effects of secondary electrons totally.

In summary, the simple models of Ref. 30 and 31 are probably incomplete and must be augmented by the effects incorporated in Ref. 44. However, this study and others show that secondary electron power is a realistic and significant influence on the discharge impedance, and hence should be included in treatments of global discharge models.

## B. Escaping Electrons

The present model omits the kinetic energy lost with escaping electrons from the electron power balance. Lieberman<sup>51</sup> introduced the instantaneous mean energy lost per escaping electron as  $2kT_e + eV_{sh}(t)$ , where  $V_{sh}(t)$  is the sheath potential surmounted by an escaping electron. Misium et al.<sup>19</sup> later showed

that the average of  $V_{sh}(t)$ , weighted by the instantaneous flux of escaping electrons, was  $-2kT_e$  for argon. (It varies slightly, decreasing logarithmically with the rf voltage in the sheath.) The mean power lost from the electrons due to this effect is therefore  $P_{esc} = 4kT_e n_s u_B$ , and this term should be added to the left side of Eq. (3). Since  $P_{esc}$  is similar in form to  $P_{loss}$ , the solution to the models remain the same except that  $E_{loss}$  is replaced by  $E_{loss} + 4kT_e$ . This correction is  $-40\%$  at 3.7 mtorr (see Table II),  $-20\%$  at 20 mtorr, and  $-10\%$  at 70 mtorr, and the trend is due to the increase of  $E_{loss}$  with pressure. Thus, this correction is most important at lower pressures and requires better treatment. At higher pressures, the use of a smaller  $\gamma_{eff}$  can compensate for the omission of  $P_{esc}$  due to the manner in which secondary electron power appears (see Eq. (34)).

We note that when escaping electrons are included in the model, the total discharge power  $P_{tot}$  must include the kinetic energy flux carried out to the electrodes by escaping electrons,  $\sum 2kT_e u_B A_i \langle n_{s,i} \rangle$ , where the symbol  $\sum$  denotes a sum over both electrodes. Thus, we have  $P_{tot} = P_{ion} + P_{loss} + \sum 2kT_e u_B A_i \langle n_{s,i} \rangle$ , where  $P_{loss}$  and  $P_{ion}$  are given by Eqs. (4) and (6), respectively. The three terms in the expression for  $P_{tot}$  account for the mechanisms that carry energy to the electrodes: Ion bombardment, recombination of ions and electrons, de-excitation of excited atoms, cooling of gas atoms, and the kinetic energy flux of escaping electrons.

Additionally, the escaping electron energy loss mechanism may require additional study: Ref. 46 reported electron kinetic energy losses at the electrodes that were roughly a third of the total electron power. These were PIC simulation results for helium discharge at 250 mtorr, from 200-800 V, at 12 MHz, and no secondary electrons were included. This is significantly greater than the  $2kT_e$  estimated above for the kinetic energy component of this loss term in the 70 mtorr case.

Wood<sup>52</sup> also showed in PIC simulations of argon discharges at 3 mtorr and 13.56 MHz that the average kinetic energy lost per escaping electron can exceed  $-2kT_e$ . The enhancement in this low pressure case is due to the loss of energetic beam electrons that have crossed the glow after being accelerated by reflection off of one expanding sheath. The simulations showed that the mean energy loss depended on the discharge length; the mean energy lost was 16.7 eV for a discharge length of 10 cm, but decreased to 10.5 and 9.2 eV

for discharge lengths of 7.5 and 13 cm, respectively. This behavior was attributed to the sensitivity of sheath heating and electron escape processes on the phase of the arrival of the beam electrons at the sheath edge.

### C. Divergence in the Density

The models presented here give a divergence in the density  $n_s(0)$ . The effect of secondary electron power should give an appreciable increase in  $n_s(0)$ . Belenguer and Boeuf<sup>53</sup> show fluid simulation results for a 3 torr helium discharge at 9.2 MHz in which the density rises from  $-2 \times 10^9 \text{ cm}^{-3}$  at 100 V, to  $-10^{10} \text{ cm}^{-3}$  at 200 V, and then rapidly to  $-10^{12} \text{ cm}^{-3}$  at 400 V. Values beyond this were not shown. At lower pressures typical of the ones used in our experiments, secondary electrons will enhance the density, but it is surprising to find a strong divergence in the density at finite voltage.

The effect of secondary electrons was studied by Godyak and Khanneh<sup>34</sup> in a work concerned with the transition of a discharge to the  $\gamma$  regime where secondary electrons principally sustain the discharge. (This happens for pressures much higher than those used in our experiment.) One result they obtained was that as the secondary electron power increased, the ionization produced by the glow electrons decreased -- that is,  $T_e$  decreased. This decrease in  $T_e$  is not present in our model because the ionization by secondary electrons has not been explicitly included in the particle balance, Eq. (2). An improvement on this model would include a term for secondary electron ionization to the particle balance, and an energy loss term for secondary electrons in the electron power balance. Including secondary electrons would then give a lower glow  $T_e$ , and this would result in a larger  $E_{\text{loss}}$ .<sup>19</sup> The voltage at which the density singularity occurs is roughly  $-E_{\text{loss}}/(e\gamma_{\text{eff}})$ , and hence a lower  $T_e$  shifts the density divergence to a higher voltage. This more complete treatment of secondary electron power would therefore reduce the rate of rise in  $I$  or  $P_{\text{tot}}$  visible in the 70 mtorr model result between 700 V and 800 V. For the 3.7 and 20 mtorr data, secondary electrons are a significant, but not the dominating electron power source. In this case,  $T_e$  and  $n_s(0)$  in the models are probably still reasonable for the level of sophistication employed here. At 70 mtorr, however, secondary electrons can contribute more power at large  $V_{\text{rf}}$  than either ohmic or stochastic heating, and a better treatment of secondary electrons becomes more important.

## VII. Summary

The first part of this paper discussed measurements of the discharge current in an asymmetric capacitive rf discharge. The current was measured at the grounded electrode, as this approach avoided measuring the current flowing through the stray capacitance from the powered electrode to ground. We found that glow confinement was crucial to accurate current measurements when the current is measured at the grounded electrode. It was also important that the electrode configuration allowed a measurement that was not sensitive to, or did not excite, current oscillations along the ground electrode surface. The procedure we have employed is somewhat equivalent to making the experimental system as simple electrically as possible. This design goal is exemplified by symmetric discharges in glass vessels.<sup>16,54</sup> These precautions are vital to impedance measurements in electropositive gases since the phase shift at 10 MHz can be just a few degrees short of  $-90^\circ$ . In such circumstances stray effects degrade the phase accuracy of the measurement.

The capacitive nature of the discharge current was verified by the measurements, and our initial method of computing the discharge current from the total current and voltage at the powered electrode was shown to be consistent with the improved current measurement procedure. These results give further evidence that the glow behaves as though its impedance has a negative resistance in argon at low pressures.

A study of the discharge impedance could be done with the new current measurements. We found a nearly linear dependence of  $I$  on  $V_{rf}$ , and a nearly quadratic dependence of the discharge power on  $V_{rf}$ . These results are similar to trends reported by others. We also found that the discharge emits power at the second harmonic.

In the second part of this paper a model of an asymmetric discharge was presented. This model represents a simplification of the work of Ref. 19; here we study the effects of including secondary electron power in the electron power balance. Also, an asymmetric electrode configuration and a nonuniform plasma density was included to test the theory of Lieberman and Savas<sup>39</sup> on the dc bias that develops between the two electrodes of an asymmetric system.

DC bias data show slight to moderate disagreement with the model (this is quantified in the discussion). The model was sensitive to the density profile and probably the degree to which the glow could

be described as a cylindrical slab. This is most likely a problem in the 3.7 mtorr, thick-sheath discharge. Another source of disagreement may be the expressions for the sheath voltages  $V_{0,i}$  and  $V_{1,i}$  used in this model. These expressions are large voltage limits for the sheath voltages, and do not incorporate the floating electrode condition explicitly in their derivation. This condition gives corrections that are important for  $V_{rf}$  up to a few hundred volts, and may thus modify the expression for the dc bias  $V_{dc}$ . This may be the major source of disagreement for the higher pressure cases, where the cylindrical slab geometry of the glow is a better approximation and hence, less of a concern.

Including secondary electron power in the electron power balance improved the linearity of  $I - V_{rf}$  relation. Effective  $\gamma_{eff}$ 's of -0.03 to -0.16 were necessary to fit the  $I - V_{rf}$  results to the experimental data. The model results for the discharge power were also found to be close to the experimental data, even though this does not automatically follow from a fit of the rf current results.

The model gives a sublinear  $I - V_{rf}$  relation when no secondary electrons are included. Adding secondary electron power to the electron power balance results in a more linear dependence of  $I$  on  $V_{rf}$ . The additional power increases the density in such a way that the sheath thickness remains relatively constant with voltage. The constant sheath thickness corresponds to a constant sheath impedance, and hence a linear  $I - V_{rf}$ . Thus, in this model, a linear  $I - V_{rf}$  relation results from the density dependence of the sheath capacitance and the power deposition mechanisms that determine the plasma density.

Other works indicate that secondary electron power is not needed to yield a linear  $I - V_{rf}$ .<sup>44,46</sup> These works imply that the sheath model employed here is not entirely correct. By the same token, such results imply that if a superlinear  $I - V_{rf}$  relation at large  $V_{rf}$  is observed, some other source of ionizing electrons, besides sheath or ohmic heating, is present. Experimental data of this sort has appeared in the literature.<sup>17</sup> Additionally, experiments by Bletzinger<sup>49</sup> show that secondary electrons have some effect on the discharge impedance even at pressures as low as 0.1 torr in argon. Thus, a model study like this is useful to understand the influence of secondary electrons on discharge behavior.

The model presented here is limited to pressures below -100 mtorr. With increasing pressure, ohmic heating becomes more important and a better value for the geometry factor  $f_G$  is needed. Also, as the

pressure rises, secondary or sheath-heated electrons will deposit their energy in a region increasingly localized near the sheath edge, and the density profile used here becomes less valid since it is based on a uniform ionization frequency.

At lower pressures than those used here, the sheath thickness will be larger, and the sheath speed  $\omega s_m$  will approach the thermal electron speed. An enhancement in the stochastic heating power is expected,<sup>52,55</sup> and this should be incorporated into the model. This was not done here because the sheath speed was not sufficiently high to make use of the large sheath speed formula derived by Wood.<sup>52</sup>

Other shortcomings of the model have been discussed, namely the need to include an energy loss term for escaping electrons, and a more complete treatment of secondary electrons in the power and particle balance. The model, however, was still able to describe the discharge impedance quite well over the voltage and pressure range investigated experimentally. It also serves to illustrate the usefulness of impedance studies: That although the discharge impedance is generally not simply related to plasma parameters like the plasma density or elastic scattering frequency as older investigations had hoped, the impedance is intimately connected with the sheath properties and the ionization processes in the discharge. Thus, experimental impedance studies can complement theoretical studies on the nature of rf sheaths and processes within the discharge.

#### **Acknowledgment**

Helpful discussions with W.B. Kunkel are gratefully acknowledged. This work was supported by NSF Grant ECS-8517363 and DOE Grant DE-FG03-87ER13727.

## References

1. T.J. Sommerer, W.N.G. Hitchon, J.E. Lawler, *Phys. Rev. Lett.* **63**, 2361 (1989).
2. A.H. Sato and M.A. Lieberman, *J. Appl. Phys.* **68**, 6117 (1990).
3. J.I. Ulacia and J.P. McVittie, *MRS Symp. Proc.* **98**, 203 (1987).
4. D.B. Ilić, *Rev. Sci. Instrum.* **52**, 1542 (1981).
5. A.J. van Roosmalen, *Appl. Phys. Lett.* **42**, 416 (1983).
6. C. Beneking, *J. Appl. Phys.* **68**, 4461 (1990).
7. V.A. Godyak, R.B. Piejak, and B.M. Alexandrovich, *J. Appl. Phys.* **69**, 3455 (1991).
8. V.A. Godyak, O.A. Popov, and A.Kh. Ganna, *Sov. J. Plasma Phys.* **2**, 560 (1976).
9. P. Bletzinger and M.J. Flemming, *J. Appl. Phys.* **62**, 4688 (1987).
10. W.G.M. van den Hoek, C.A.M. de Vries, and M.G.M. Heijman, *J. Vac. Sci. Technol. B* **5**, 647 (1987)
11. C.M. Horwitz, *J. Vac. Sci. Technol. A* **1**, 1795 (1983).
12. K.E. Greenberg, P.J. Hargis, and P.A. Miller, Sandia National Laboratories internal report SETEC 90-013, Nov. 1990.
13. S.E. Savas, D.E. Horne, R.W. Sadowski, *Rev. Sci. Instrum.* **57**, 1248 (1986).
14. V.A. Godyak and R.B. Piejak, *J. Vac. Sci. Tech. A* **8**, 3833 (1990).
15. J.W. Butterbaugh, L.D. Baston, and H.H. Sawin, *J. Vac. Sci. Technol. A* **8**, 916 (1990).
16. V.M. Donnelly, D.L. Flamm, and R.H. Bruce, *J. Appl. Phys.* **58**, 2135 (1985).
17. V.A. Godyak, R.B. Piejak, and B.M. Alexandrovich, *IEEE Trans. Plasma Sci.* **19**, 660 (1991).
18. A. Mitchell and R.A. Gottscho, *J. Vac. Sci. Technol. A* **8**, 1712 (1990).
19. G.R. Misium, A.J. Lichtenberg, M.A. Lieberman, *J. Vac. Sci. Technol. A* **7**, 1007 (1989).
20. F. Tochikubo, T. Kokubo, S. Kakuta, A. Suzuki, and T. Makabe, *J. Phys. D* **23**, 1185 (1990).
21. J.H. Keller and W.B. Pennebaker, *IBM J. Res. Devel.* **23**, 3 (1979).
22. J. S. Logan, J. Constable, F. Jones, J.E. Lucy, *J. Vac. Sci. Technol. A* **8**, 1835 (1990).
23. *Reference Data for Radio Engineers*, (Howard W. Sams & Co., Inc.; Indianapolis, Indiana; 1981), p. 4-28.

24. A.H. Sato and M.A. Lieberman, Memorandum No. UCB/ERL M91/81, 25 Sept. 1991, Electronics Research Laboratory, College of Engineering, University of California, Berkeley, 94720. Submitted to *Journal of Applied Physics*.
25. M. Surendra and D.B. Graves, *Phys. Rev. Lett.* **66**, 1469 (1991).
26. V.A. Godyak and A.A. Kuzovnikov, *Sov. J. Plasma Phys.* **1**, 276 (1975).
27. B. Chapman, *Glow Discharge Processes*, (Wiley, New York, 1980), pp. 87-88.
28. Gavin C.H. Zau, Jeffrey W. Butterbaugh, Paul Rummel, and Herbert H. Sawin, *J. Electrochem. Soc.* **138**, 872 (1991).
29. A.H. Sato, *IEEE Trans. Plasma Sci.* **19**, 214 (1991).
30. M.A. Lieberman, *IEEE Trans. Plasma Sci.* **16**, 638 (1988).
31. M.A. Lieberman, *IEEE Trans. Plasma Sci.* **17**, 338 (1989).
32. V.A. Godyak and O.A. Popov, *Sov. J. Plasma Phys.* **5**, 227 (1979).
33. O.A. Popov and V.A. Godyak, *J. Appl. Phys.* **57**, 53 (1985).
34. V.A. Godyak and A.S. Khanneh, *IEEE Trans. Plasma Sci.* **14**, 112 (1986).
35. P.F. Little, in *Handbuch der Physik*, edited by S. Flügge (Springer-Verlag, Berlin, 1956), Vol. 21, pp. 574-663.
36. B. Szapiro and J.J. Rocca, *J. Appl. Phys.* **65**, 3713 (1989).
37. V.A. Godyak, *Sov. J. Plasma Phys.* **2**, 78 (1976).
38. F. Schneider, *Z. Angew. Phys.* **6**, 456 (1954). Also, S.M. Levitskii and I.P. Shashurin, *Sov. Phys. Tech. Phys.* **8**, 319 (1963).
39. M.A. Lieberman and S.E. Savas, *J. Vac. Sci. Technol. A* **8**, 1632 (1990).
40. This is similar to the expression given in V.A. Godyak and A. KH. Ganna, *Sov. J. Plasma Phys.* **5**, 376 (1979), differing by the factor of  $3^{-0.5}$ .
41. George R. Misium, thesis, University of California, Berkeley, 1988.
42. V.A. Godyak, *Phys. Lett.* **89A**, 80 (1982).
43. E.W. McDaniel, *Collisional Phenomena in Ionized Gases*, (Wiley, New York, 1964), p.164.

44. V.A. Godyak and N. Sternberg, *Phys. Rev. A* **42**, 2299 (1990).
45. G.R. Misium, *J. Vac. Sci. Technol. A* **8**, 1642 (1990).
46. M. Surendra and D.B. Graves, *IEEE Trans. Plasma Sci.* **19**, 144 (1991).
47. P. Mirrashidi, B.P. Wood, V. Vahedi, M.A. Lieberman, and C.K. Birdsall, Poster DB-9, 44<sup>th</sup> Annual Gaseous Electronics Conference, 22-25 October 1991, Albuquerque, New Mexico.
48. M.J. Kushner, *IEEE Trans. Plasma Sci.* **14**, 188 (1986).
49. P. Bletzinger, *J. Appl. Phys.* **67**, 130 (1990).
50. M. Surendra, D.B. Graves, and I.J. Morey, *Appl. Phys. Lett.* **56**, 1022 (1990).
51. M.A. Lieberman, Memorandum No. UCB/ERL M87/65, 7 Sept. 1987, Electronics Research Laboratory, College of Engineering, University of California, Berkeley, 94720.
52. B.P. Wood, Ph.D. dissertation, University of California, Berkeley, 1991.
53. Ph. Belenguer and J.P. Boeuf, *Phys. Rev. A* **41**, 4447 (1990).
54. V.A. Godyak, R.B. Piejak, and B.M. Alexandrovich, *Rev. Sci. Instrum.* **61**, 2401 (1990).
55. D. Vender and R.W. Boswell, *IEEE Trans. Plasma Sci.* **18**, 725 (1990).

**Table I.** Phase angle of the discharge impedance at the second harmonic. The experimental data appears in the third column, and results from the two-sheath model appear in the fourth through sixth columns.  $kT_e/e$  used in the model computations is given in the seventh column.

pressure (mtorr)	$V_{rf}$ (volt)	exp't	model phase (deg.)			
		phase (deg.)	at density parameter of:			
			$10^9 \text{ cm}^{-3}$	$10^{10} \text{ cm}^{-3}$	$23 \times$ $10^9 \text{ cm}^{-3}$	$kT_e/e$ (volt)
3.8	145	112	90	100	---	4
3.8	700	115	97	100	117	4
20	120	99	87	96	---	2.6
20	700	104	95	98	112	2.6
70	102	95	84	93	---	2
70	700	100	94	97	112	2

TABLE II. Parameter values used in the model computations. The index  $p$  in column 10 refers to the collisionless ( $p=1/2$ ) or collisional ( $p=2/5$ ) sheath models.  $G_p$  and  $F_p$  are evaluated at  $a/\lambda_{01}$  and  $2b/\pi$ , respectively.

$P$ (mtorr)	$\lambda_i$ (cm)	$R$ (cm)	$L$ (cm)	$a$	$b$	$kT_e$ (eV)	$E_{loss}$ (eV)	$K_m$ ( $10^{-13}$ $m^3/s$ )	$P$ in $\langle P \rangle$	$G_p$	$F_p$	$f_G$
3.7	1.0	10.7	-4.2	1.52	0.9191	-4.0	42	1.2	1/2	0.162	0.543	1.6
20	0.2	10.8	-4.8	2.16	-1.09	-2.6	52	0.78	1/2	0.282	0.622	2.3
20	0.2	10.8	-5.3	2.16	-1.11	-2.6	52	0.76	2/5	0.301	0.645	2.3
70	.06	11.0	-5.5	2.2	-1.41	-1.8	72	0.47	2/5	0.307	0.763	3.1

**TABLE III.** Comparison of the ion mean free path  $\lambda_i$  and the model results for the sheath thicknesses (on axis) at the powered and grounded electrodes.

<b>p</b> <b>(mtorr)</b>	<b><math>\lambda_i</math></b> <b>(cm)</b>	<b><math>s_{m,pe}(0)</math></b> <b>(cm)</b>	<b><math>s_{m,gc}(0)</math></b> <b>(cm)</b>
3.7	1.05	1.2 - 1.6	0.6 - 0.7
20 (collisionless)	0.20	1.0 - 1.2	0.28 - 0.4
20 (collisional)	0.20	0.58 - 0.83	0.25 - 0.36
70	0.056	0.46 - 0.63	0.21 - .03

**TABLE IV.** Comparison of the slopes of the dc bias,  $V_{dc}$ , vs. rf voltage,  $V_{rf}$ .

slope of $V_{dc}$ vs. $V_{rf}$			
p (mtorr)	model	experiment	(exp't - model) / (exp't)
3.7	0.47	0.35	-34%
20	0.45 (collisional)	0.54	+17%
70	0.42	0.50	+16%

### Figure Captions

Figure 1. The vacuum chamber and electrode configuration. A: rf power supply. B: blocking capacitor. C: directional wattmeter. D: matching network. E: capacitive divider. GE1: original grounded electrode. GE2: new grounded electrode for the confined glow experiments.

Figure 2. Using two gated integrator and boxcar averager modules for the current and voltage measurements. The triggering scheme is indicated.

Figure 3. Current waveforms. (a) Total current  $I_{tot}(t)$  measured at the powered electrode, the current through the stray capacitance  $C_s$   $dV/dt$ , and the discharge current  $I(t)$  computed from  $I_{tot}$ . The rf voltage  $V(t)$  is shown for reference. The conditions are: 30 mtorr; nominal voltage amplitude is 600 V. (b) Discharge current measured at the new grounded electrode in the confined glow experiments. Conditions are: 20 mtorr, 600 V.

Figure 4. Discharge current  $I(t)$  and the axial electric field in the original vacuum chamber configuration. Conditions are: 2.3 mtorr, 600 V rf amplitude, 3 inch electrode spacing. The electric field measurements are taken at three positions in the glow:  $\Delta$  0.875 inch,  $\circ$  1.75 inch, and  $\square$  2.625 inches from the powered electrode. Typical error bars are indicated for the 0.875 inch points only. The rf voltage  $V(t)$  is shown for reference.

Figure 5. Data for the 3.7 mtorr argon discharge. (a) dc bias. (b) first harmonic current amplitude. (c) total discharge power. Experimental data: dots. Collisionless sheath model:  $\gamma_{eff} = 0$  (dashed line), 0.03 (solid line). The abscissa gives the first harmonic voltage amplitude.

Figure 6. Data for the 20 mtorr discharge. (a) dc bias. (b) first harmonic current amplitude. (c) total discharge power. Experimental data: dots. Collisional sheath model:  $\gamma_{\text{eff}} = 0$  (dashed line), 0.08 (solid line). Collisionless sheath model result for  $\gamma_{\text{eff}} = 0.125$ : free fall.

Figure 7. Data for the 70 mtorr discharge. (a) dc bias. (b) first harmonic current amplitude. (c) total discharge power. Experimental data: dots. Collisional sheath model:  $\gamma_{\text{eff}} = 0$  (dashed line), 0.16 (solid line).

Figure 8. Current and voltage amplitude spectra for the 70 mtorr, 700 V argon discharge in the confining electrode configuration. (The dc bias has been omitted from this plot.)

Figure 9. (a) Equivalent resistance R, and (b) equivalent capacitance C for the discharge impedance at the first harmonic. Dots: 3.7 mtorr. Squares: 20 mtorr. Triangles: 70 mtorr.

Figure 10. Phase of the discharge impedance at the first harmonic. The dots are experimental data. (a) 3.7 mtorr data and collisionless sheath model result with  $\gamma_{\text{eff}} = 0.03$ . (b) 20 mtorr data and collisional model result,  $\gamma_{\text{eff}} = 0.08$ . (c) 70 mtorr data and collisional model result,  $\gamma_{\text{eff}} = 0.16$ .

Figure 11. Collisionless sheath model results for the sheath thickness at the powered and grounded electrodes, with ( $\gamma_{\text{eff}} = 0$ ) and without ( $\gamma_{\text{eff}} = 0.03$ ) secondary electrons, for the 3.7 mtorr case. The values for  $\gamma_{\text{eff}}$  label each curve.

Figure 12. Comparison of ion and electron power contributions. Collisional sheath model results for the 20 mtorr case. In (a)  $P_{\text{ion}}$  is given by "ion";  $P_{\text{st}}$  is given by 1. In (b)  $P_{\text{st}}$ ,  $P_{\text{sec}}$ ,  $P_{\text{ohm}}$  are given by 1, 2, and 3 respectively.

Figure 13. Comparison of the contributions to the electron power for (a) the 3.7 mtorr (collisionless sheath model) and (b) the 70 mtorr (collisional sheath model) cases.  $P_{st}$ ,  $P_{sec}$ ,  $P_{ohm}$  are given by 1, 2, and 3 respectively.

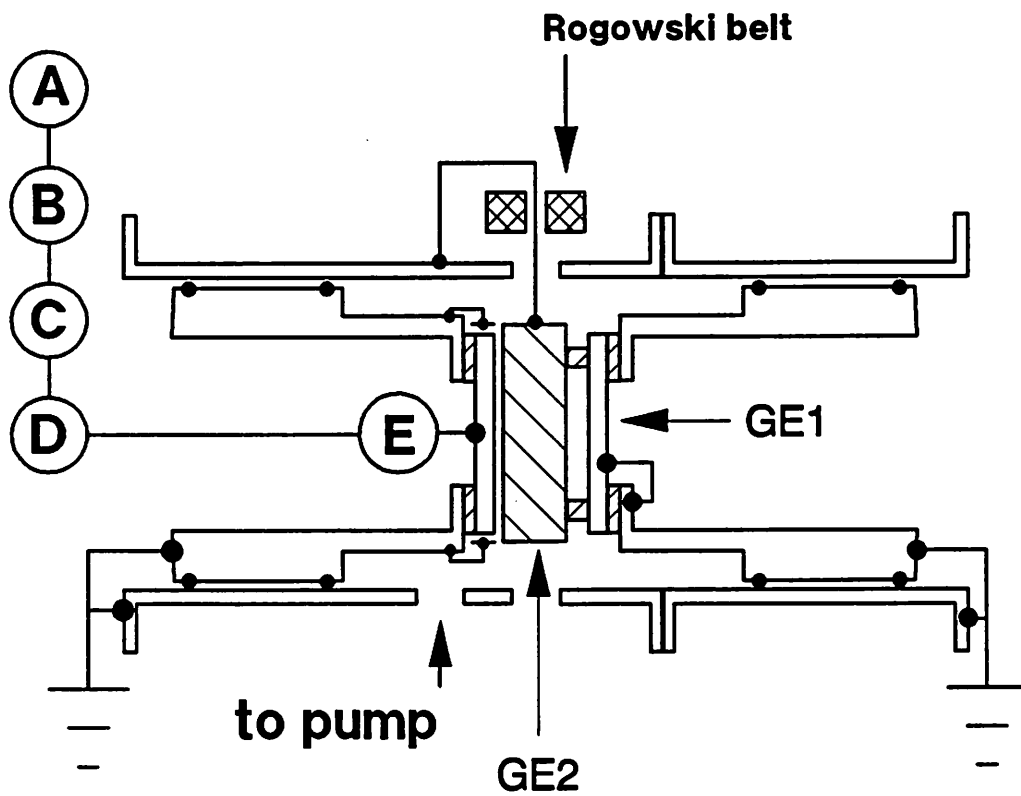


Figure 1

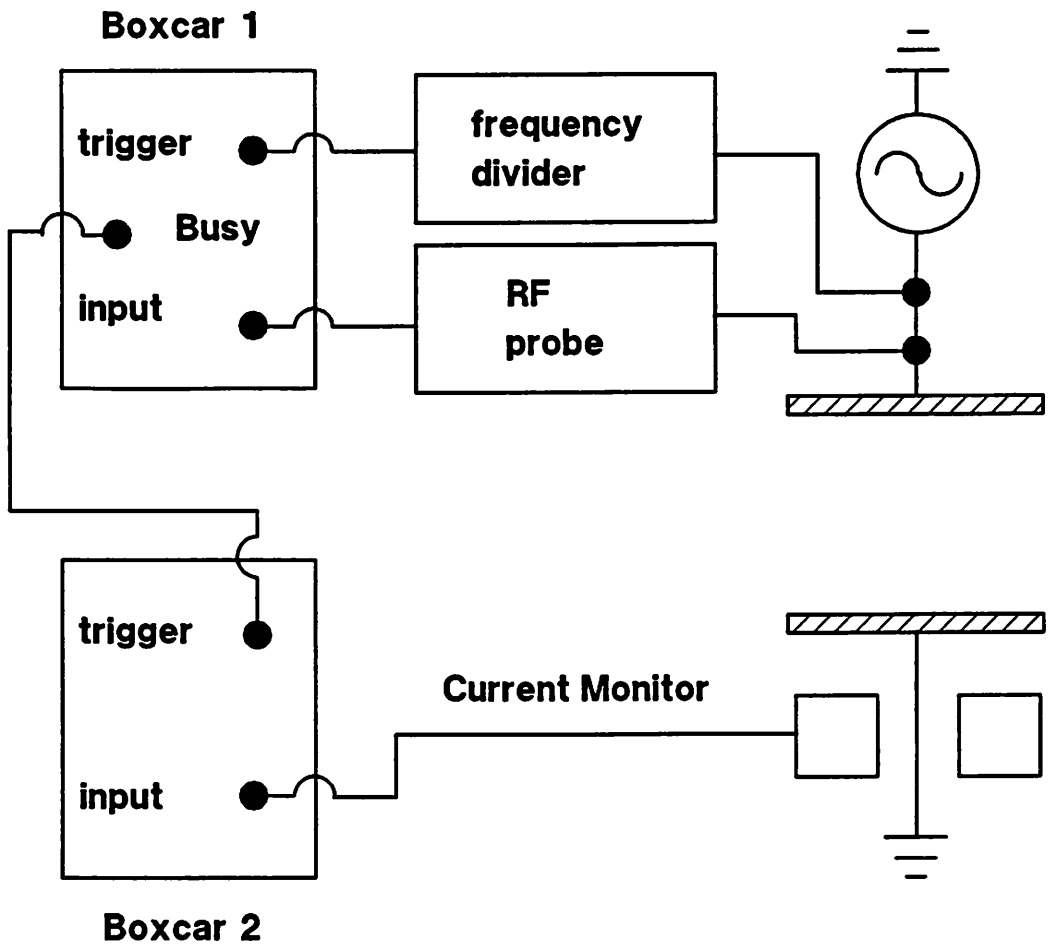


Figure 2

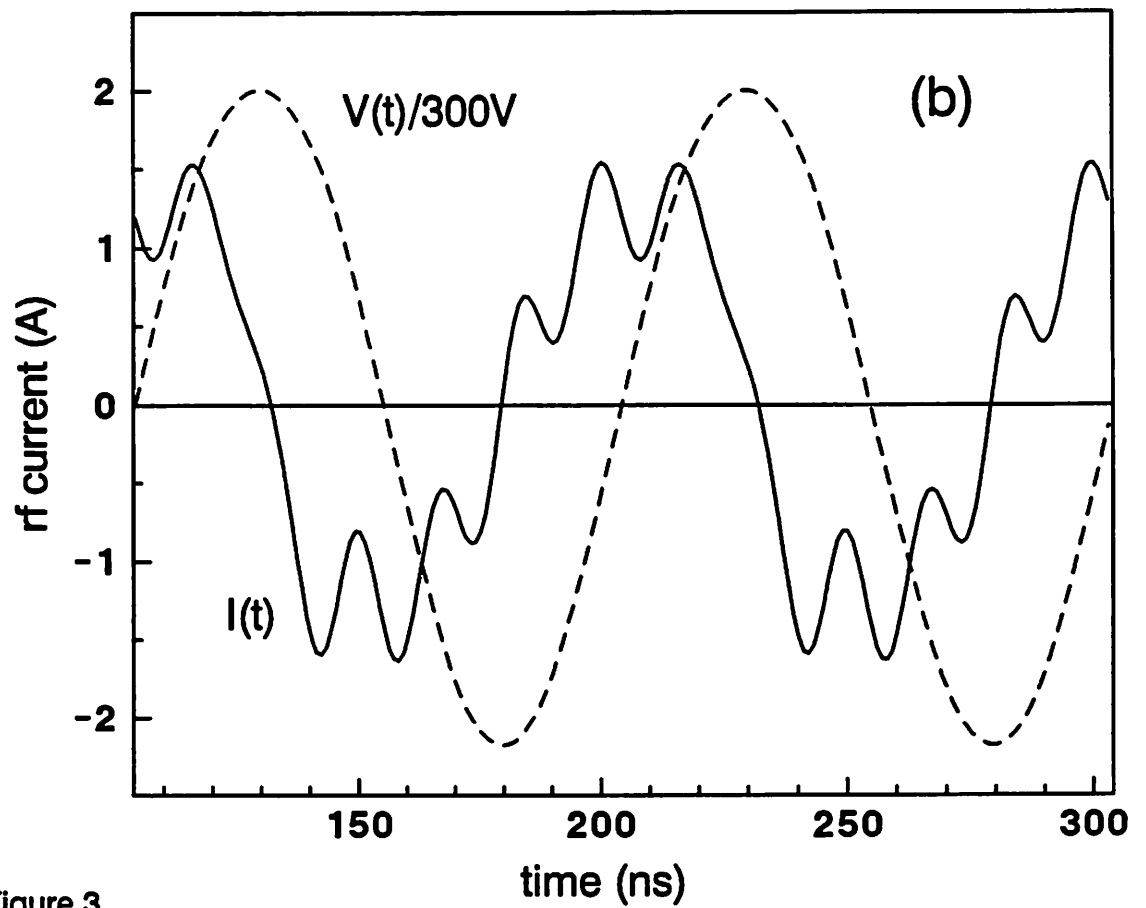
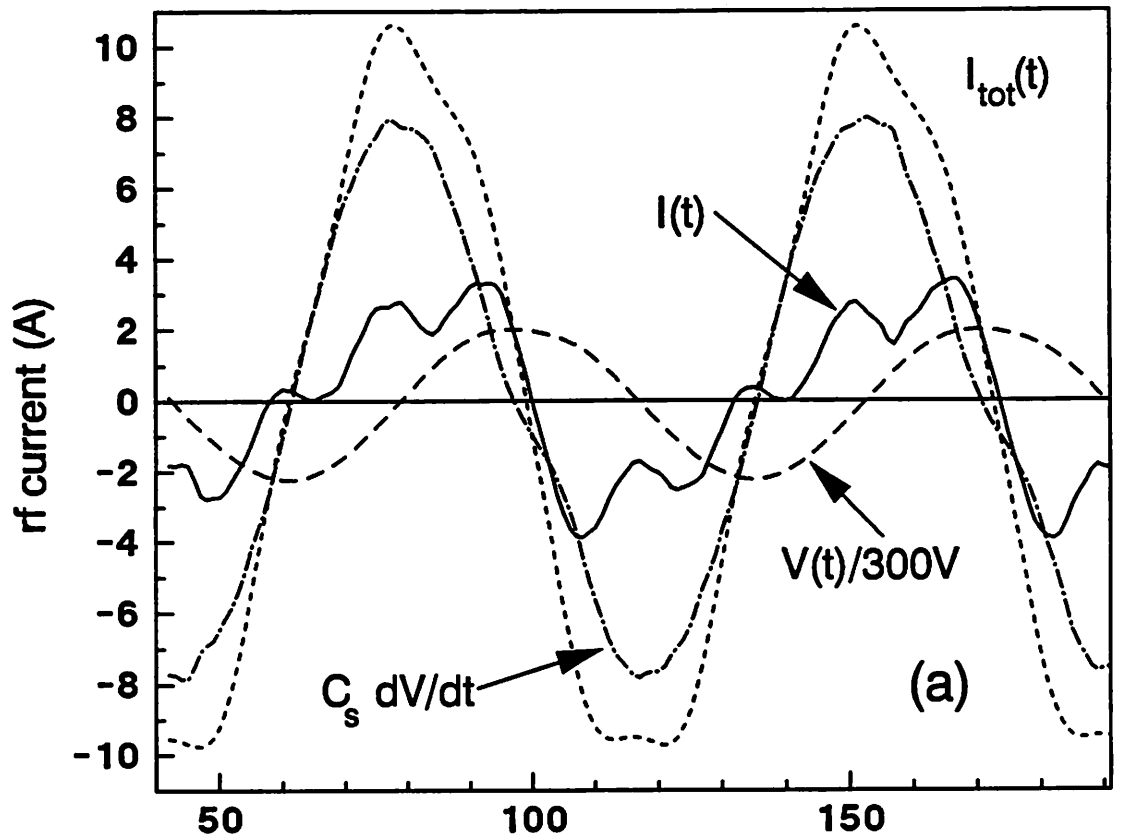


Figure 3

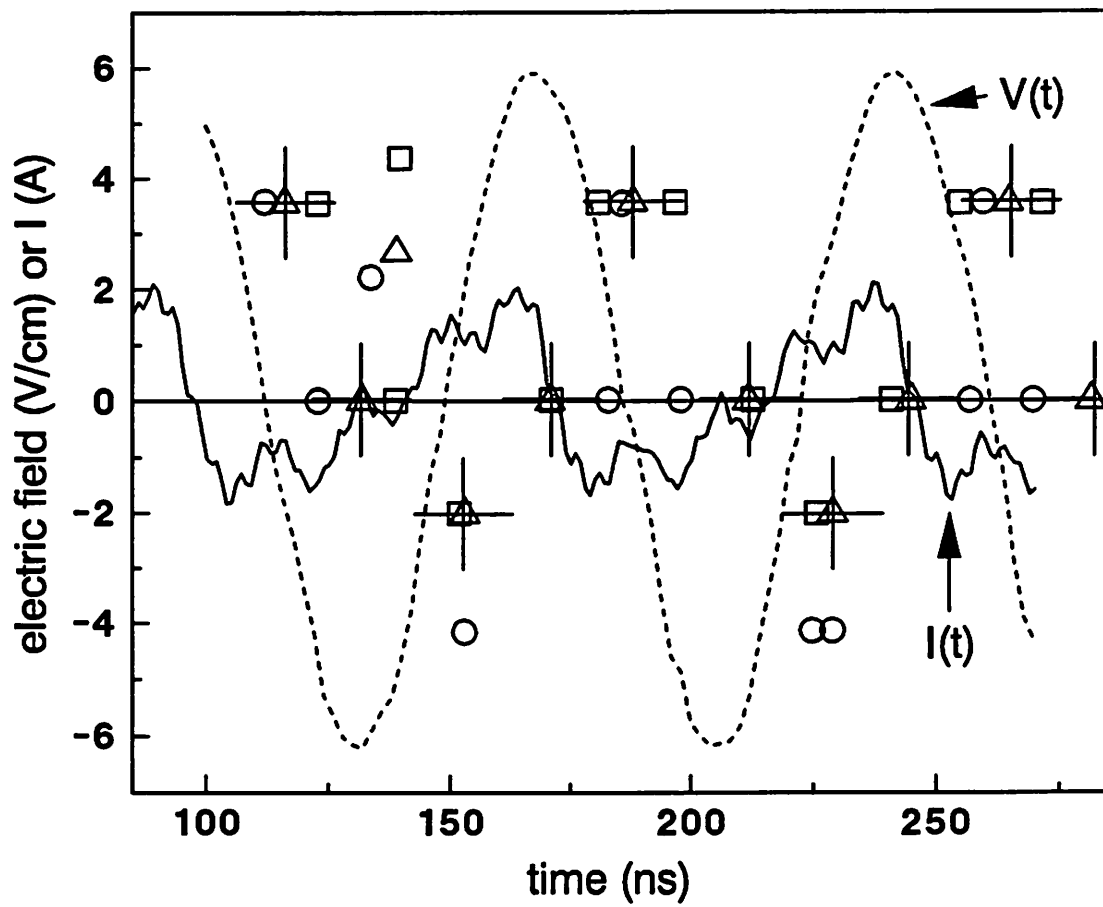


Figure 4

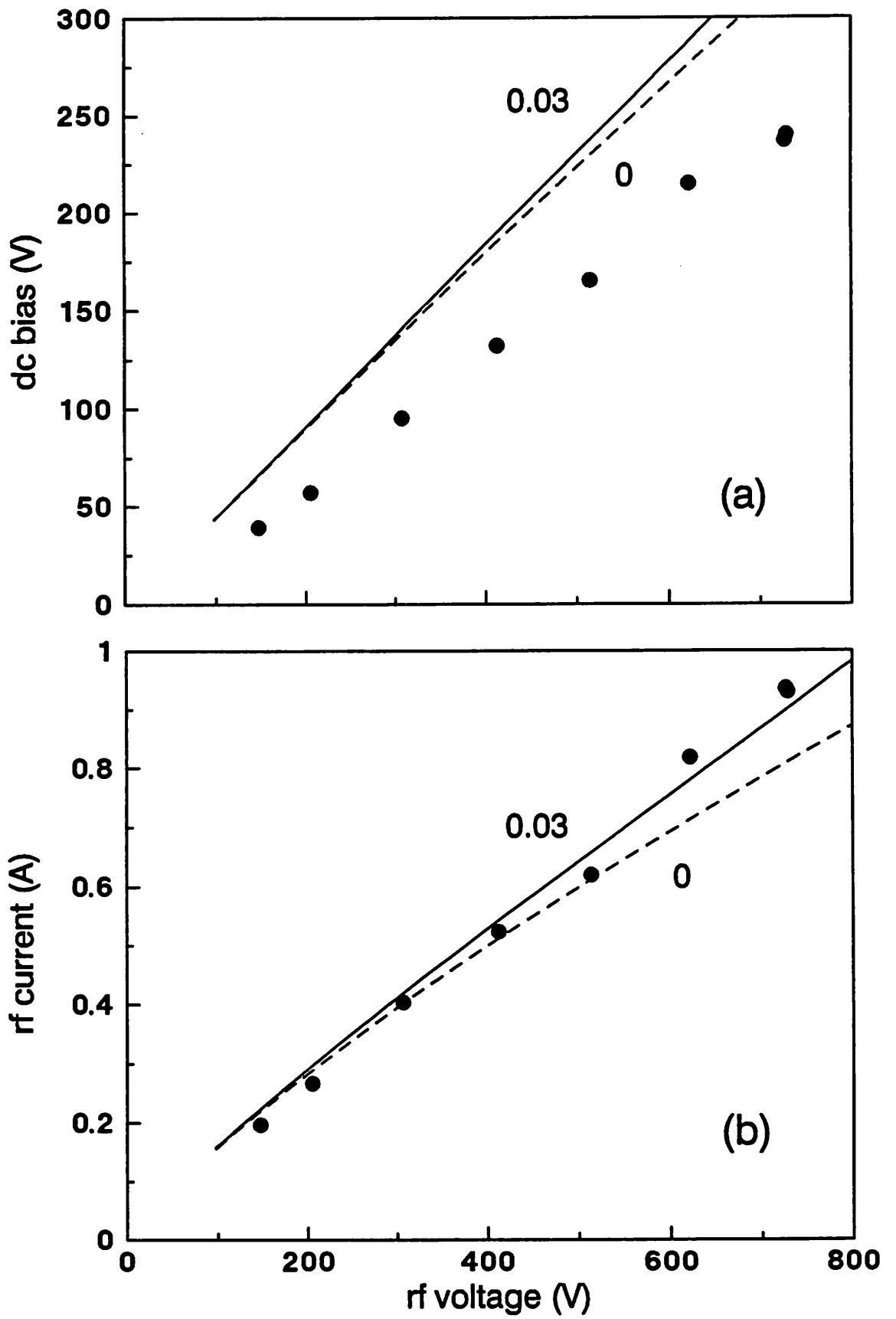


Figure 5

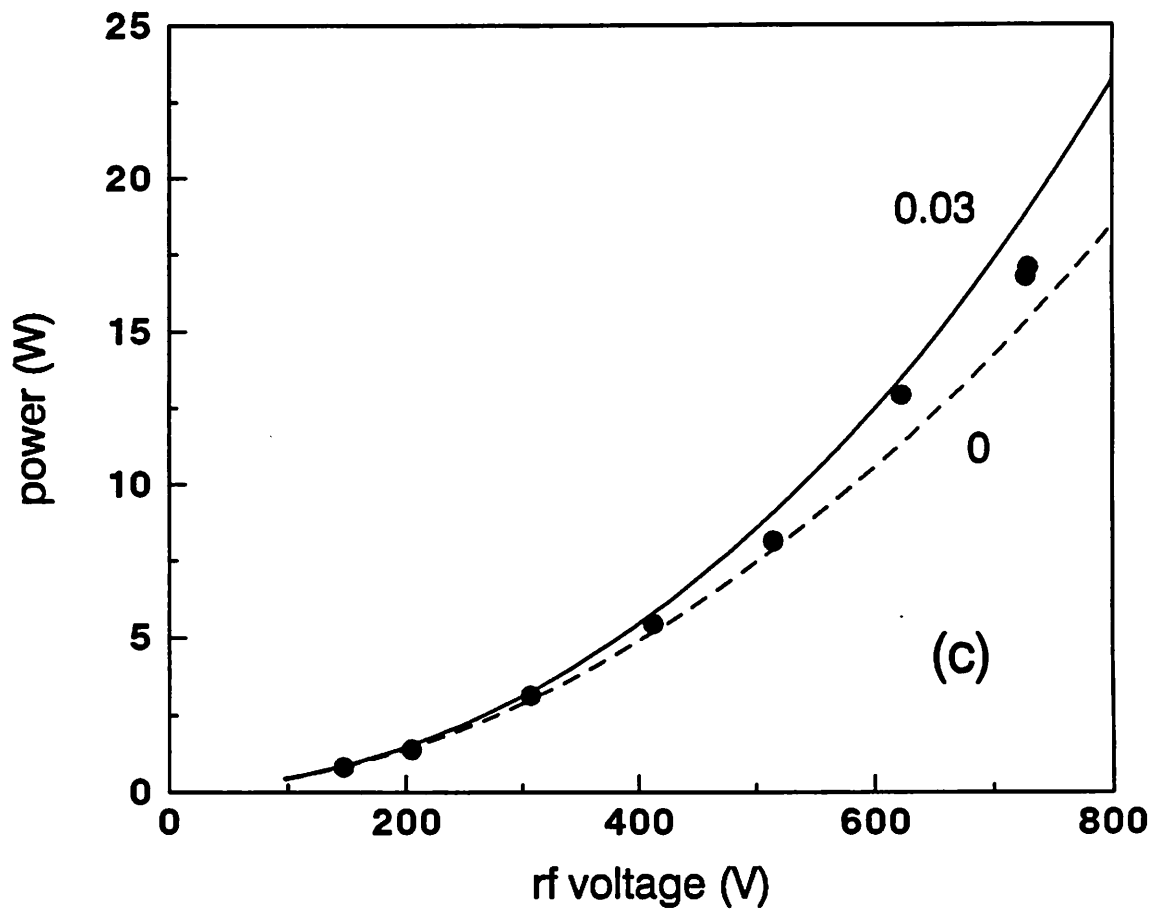


Figure 5 (con'd)

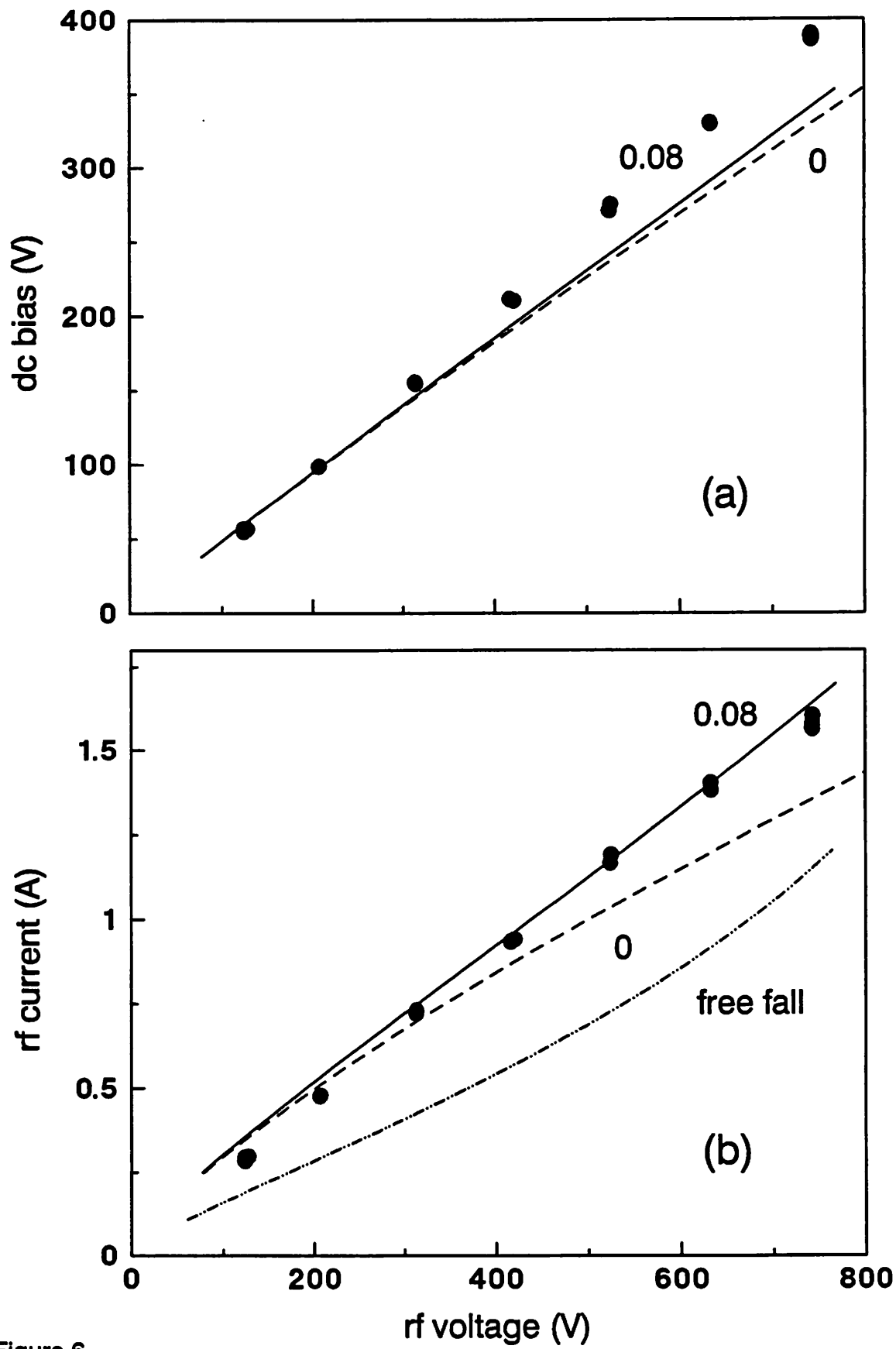


Figure 6

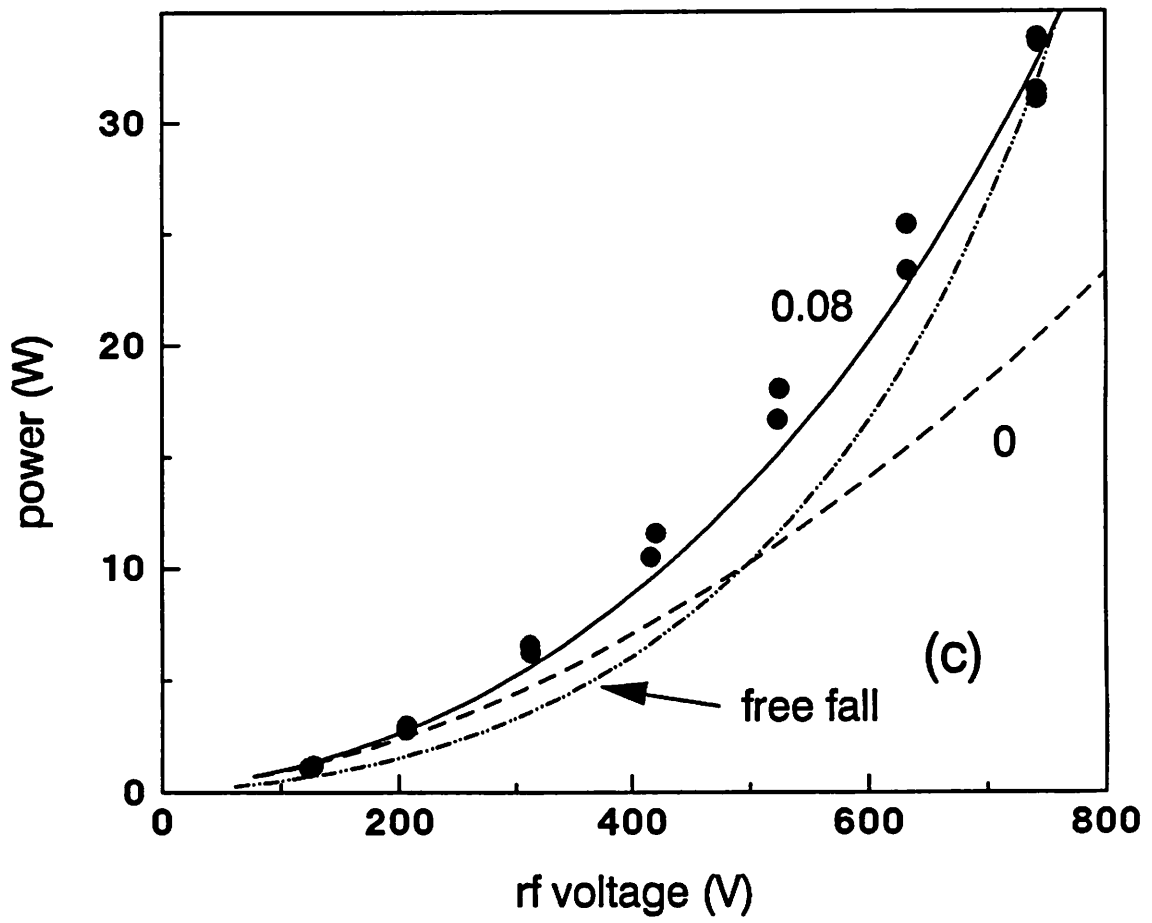


Figure 6 (con'd)

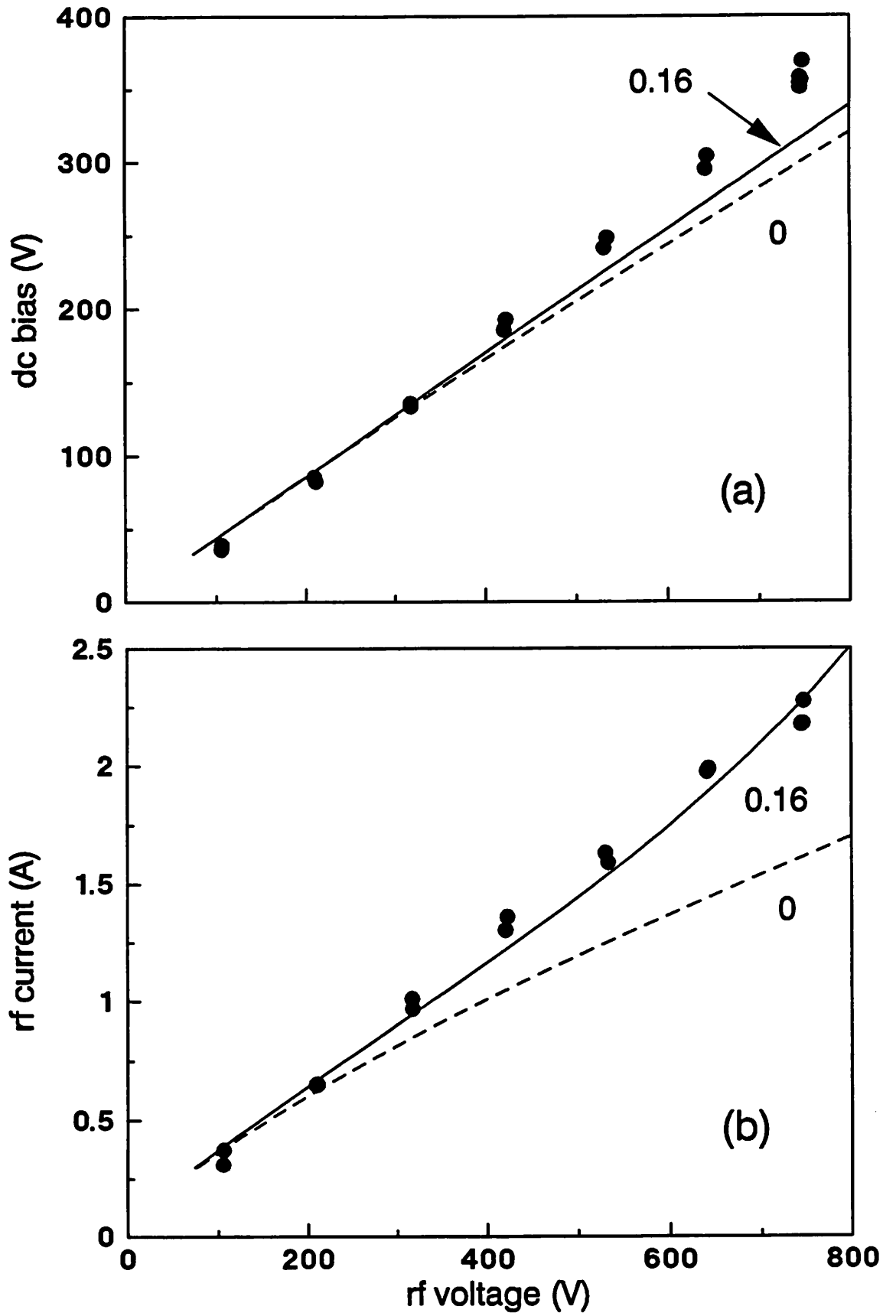


Figure 7

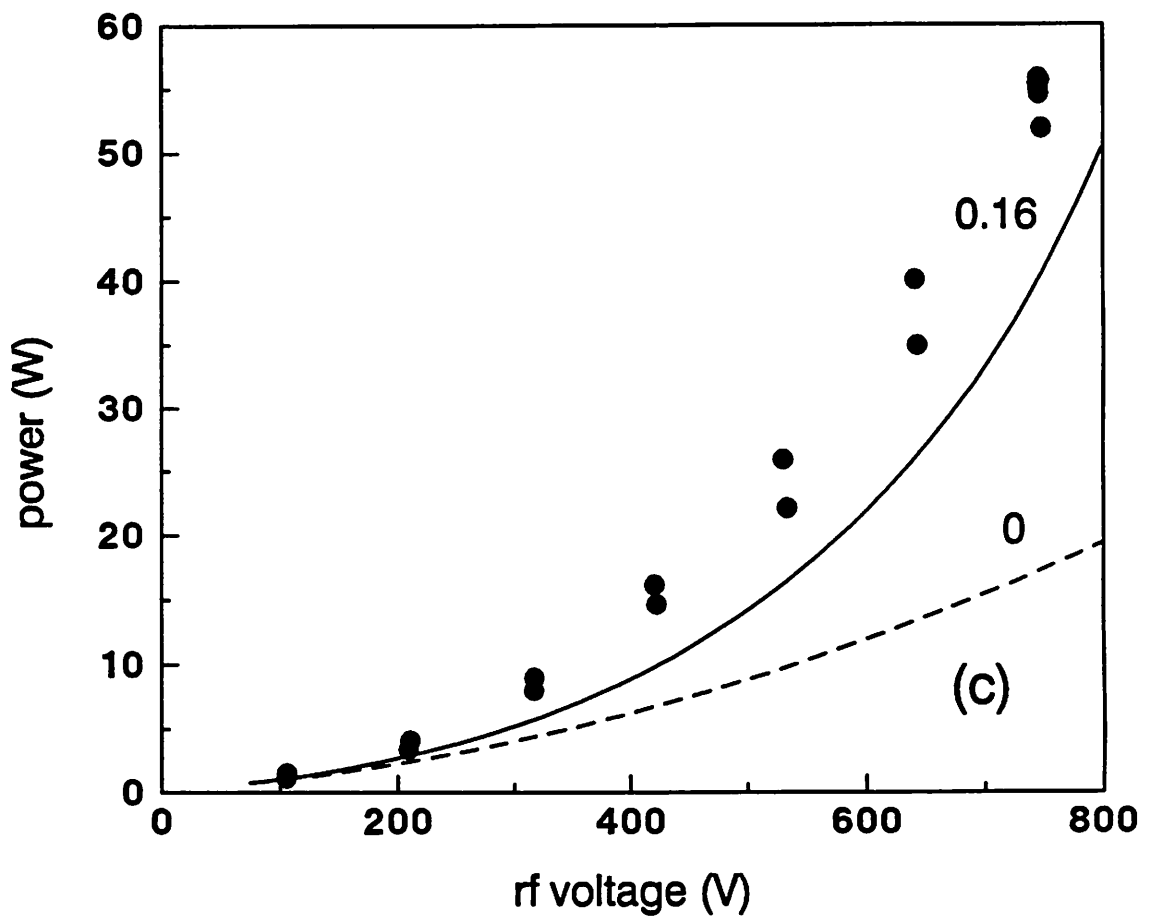


Figure 7 (con'd)

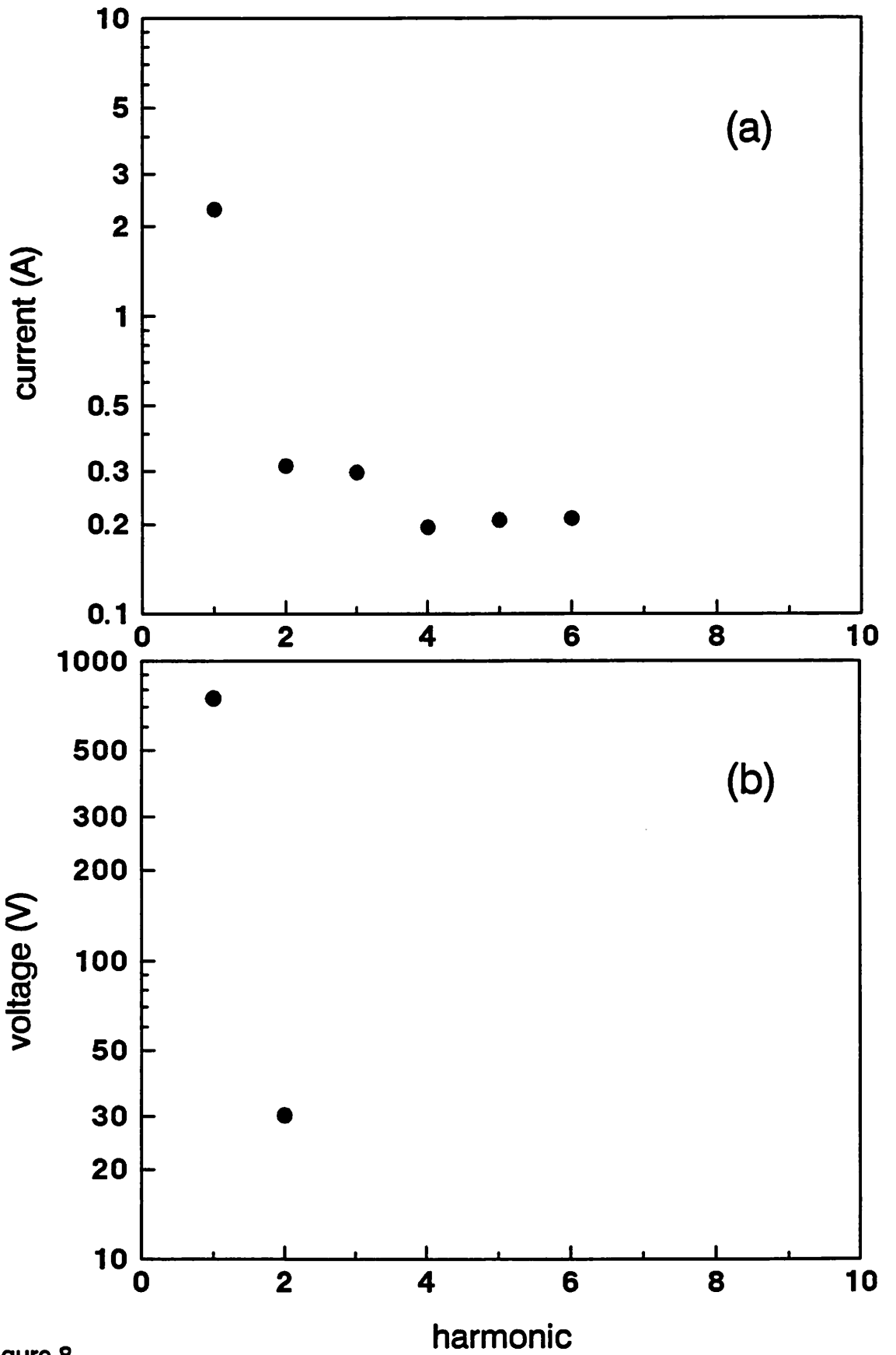


Figure 8



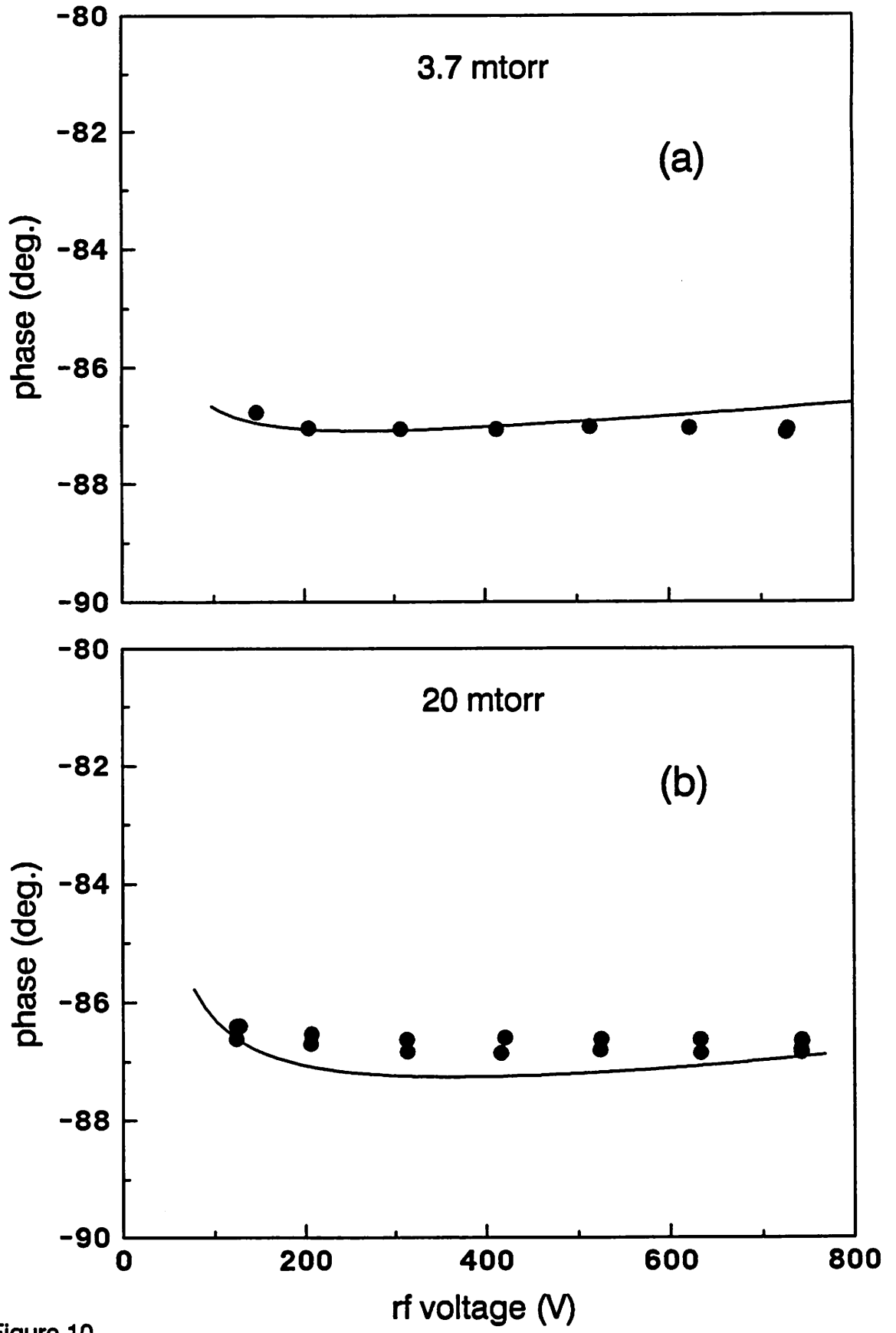


Figure 10

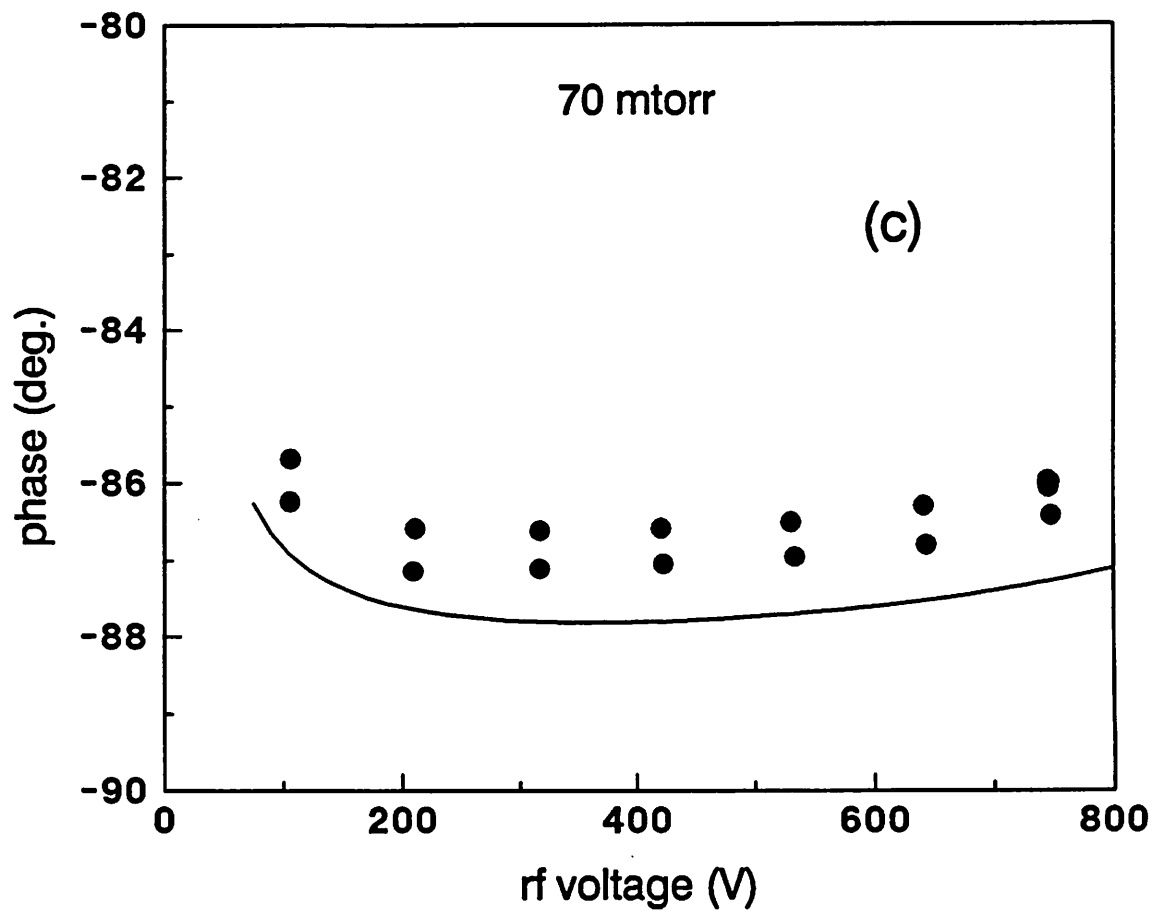


Figure 10 (con'd)

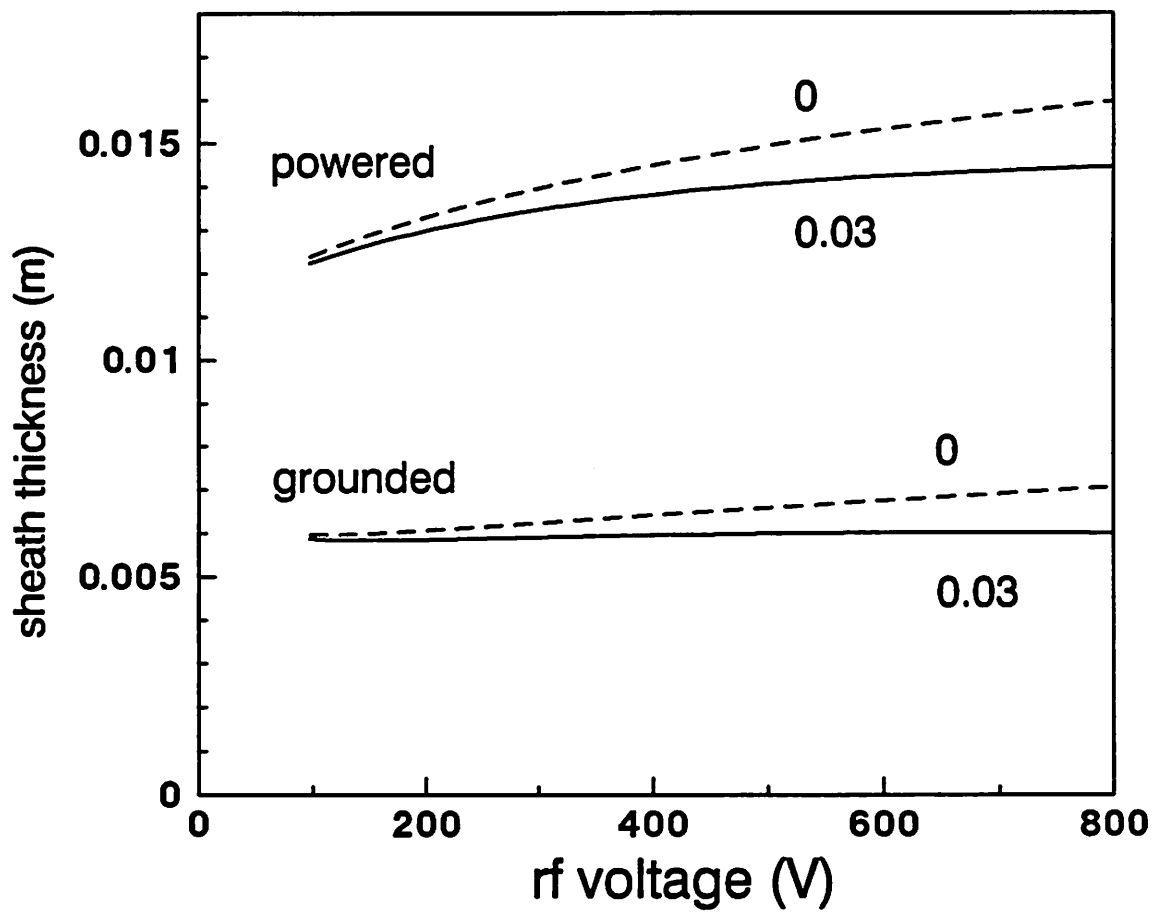


Figure 11

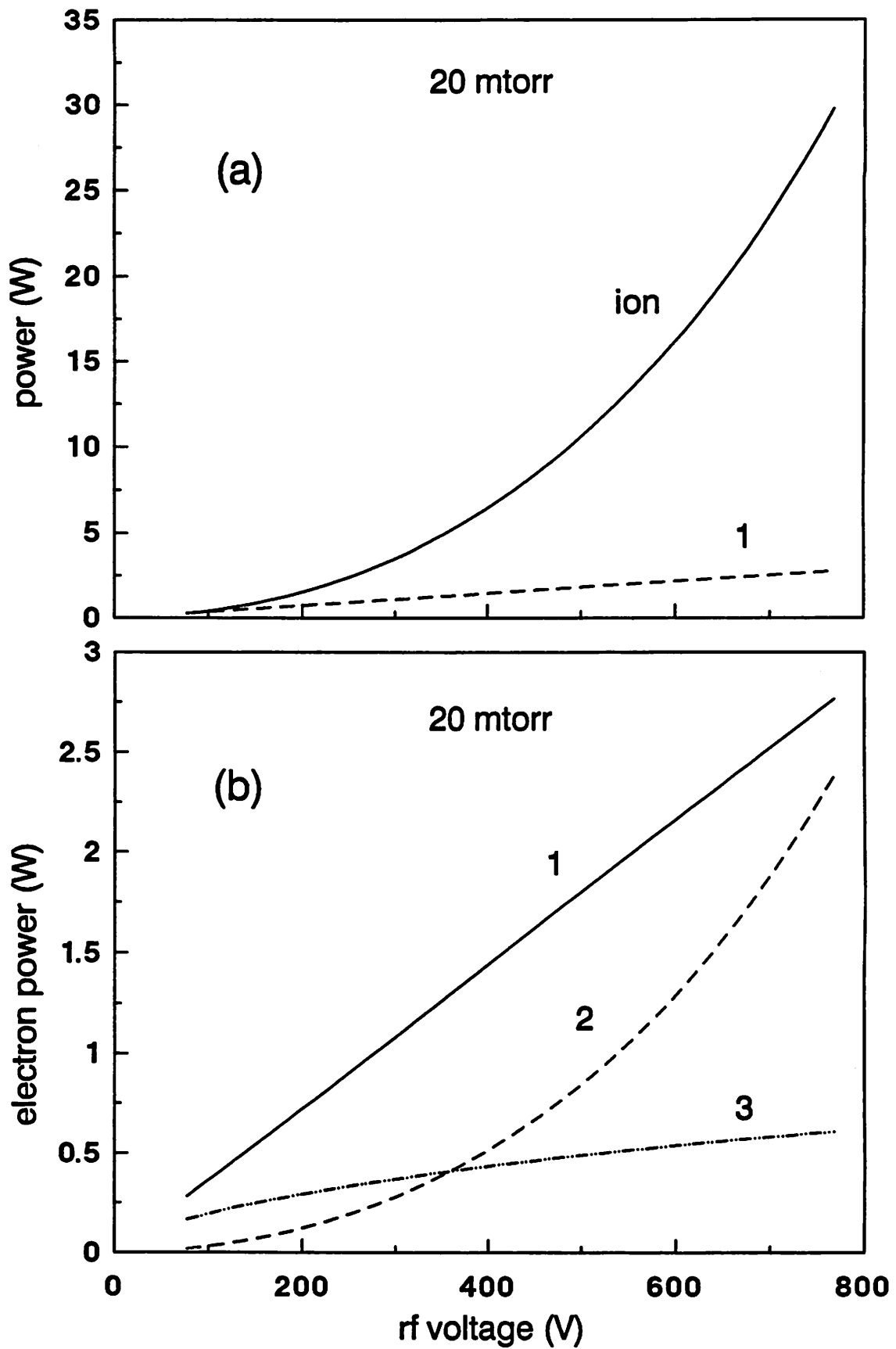


Figure 12

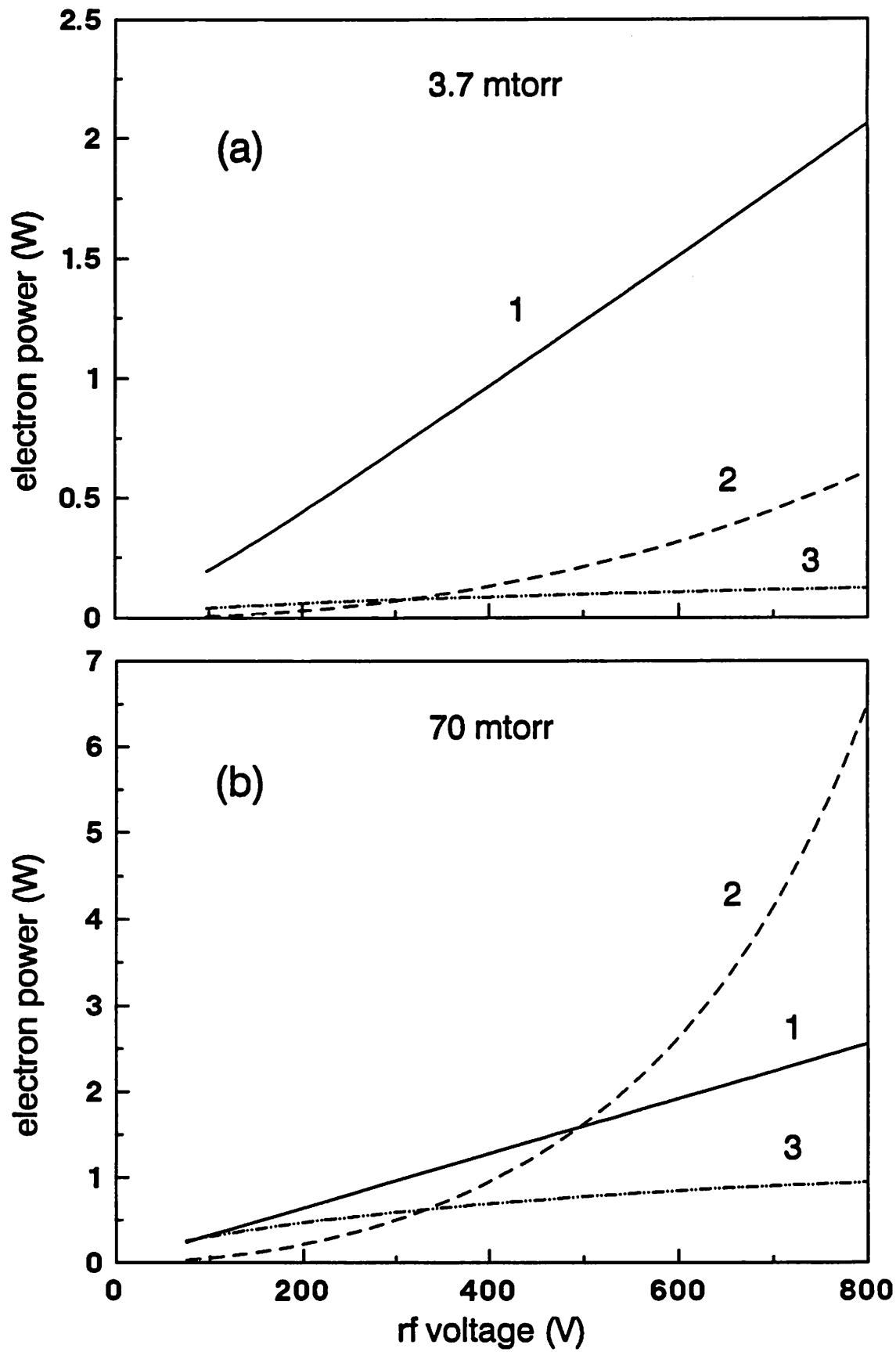


Figure 13